

MIT Open Access Articles

Mixing dry and wet magmas in the lower crust of a continental arc: new petrological insights from the Bear Valley Intrusive Suite, southern Sierra Nevada, California

The MIT Faculty has made this article openly available. **Please share** how this access benefits you. Your story matters.

Citation: Contributions to Mineralogy and Petrology. 2021 Sep 01;176(9):73

As Published: <https://doi.org/10.1007/s00410-021-01832-2>

Publisher: Springer Berlin Heidelberg

Persistent URL: <https://hdl.handle.net/1721.1/136885>

Version: Author's final manuscript: final author's manuscript post peer review, without publisher's formatting or copy editing

Terms of use: Creative Commons Attribution-Noncommercial-Share Alike



Mixing dry and wet magmas in the lower crust of a continental arc: new petrological insights from the Bear Valley Intrusive Suite, southern Sierra Nevada, California

Cite this Accepted Manuscript (AM) as Accepted Manuscript (AM) version of Hervé Rezeau, Benjamin Z. Klein, Oliver Jagoutz, Mixing dry and wet magmas in the lower crust of a continental arc: new petrological insights from the Bear Valley Intrusive Suite, southern Sierra Nevada, California, Contributions to Mineralogy and Petrology <https://doi.org/10.1007/s00410-021-01832-2>

This AM is a PDF file of the manuscript accepted for publication after peer review, when applicable, but does not reflect post-acceptance improvements, or any corrections. Use of this AM is subject to the publisher's embargo period and AM terms of use. Under no circumstances may this AM be shared or distributed under a Creative Commons or other form of open access license, nor may it be reformatted or enhanced, whether by the Author or third parties. See here for Springer Nature's terms of use for AM versions of subscription articles: <https://www.springernature.com/gp/open-research/policies/accepted-manuscript-terms>

The Version of Record of this article, as published and maintained by the publisher, is available online at: <https://doi.org/10.1007/s00410-021-01832-2>. The Version of Record is the version of the article after copy-editing and typesetting, and connected to open research data, open protocols, and open code where available. Any supplementary information can be found on the journal website, connected to the Version of Record.

Mixing dry and wet magmas in the lower crust of a continental arc: New petrological insights from the Bear Valley Intrusive Suite, southern Sierra Nevada, California

Hervé Rezeau^{1*}, Benjamin Z. Klein^{1,2} and Oliver Jagoutz¹

¹Department of Earth, Planetary and Atmospheric Sciences, Massachusetts Institute of Technology, 77 Massachusetts Avenue, Cambridge, MA 02139, USA

²Institute of Earth Sciences, Géopolis 4897, CH-1015 Lausanne, Switzerland

*Corresponding author: hrezeau@mit.edu

Abstract

Exposures of arc crustal sections represent rare opportunities to directly evaluate lower crustal magmatic processes and their link to arc products in the middle and upper crust. Within the southernmost Sierra Nevada Batholith, the Bear Valley Intrusive Suite (BVIS) exposes a contemporaneously constructed ~30 km thick intrusive suite, and thus is ideal for this type of examination. Here we present detailed petrography and mineral major and trace element data for the BVIS. The deepest exposed portion of the BVIS (8-9 kbars) is composed of heterogeneous mafic igneous intrusions of olivine metagabbro, olivine-hornblende orthopyroxenite, olivine-bearing hornblende norite, hornblende norite, hornblende gabbro, hornblende gabbro, hornblende norite, hornblende gabbro. Shallower crustal intrusions (3-7 kbars) are comparatively homogeneous and dominated by hypersthene-bearing and hypersthene-free tonalites. Using amphibole-plagioclase geothermometry, we show that the mafic lower crustal intrusions crystallized over a wide temperature range from 850-1070°C, highlighting mafic igneous fractionation during isobaric cooling in lower crust of the Sierran arc, while tonalitic liquids were emplaced at temperatures <800 °C in the middle to upper crust. Calculated trace element melt compositions in equilibrium with amphibole in lower crustal gabbros are similar to measured tonalite bulk compositions and support the generation of tonalites through fractionation of the observed gabbros. Further, petrography and mineral chemistry suggest multiple distinct crystallization sequences recorded in the different types of gabbro, requiring the presence of coexisting parental melts with contrasting compositions and H₂O contents. Using available experimental data, we develop a model by which mixing of variably fractionated dry and wet magmas with similar viscosities followed by crystallization-differentiation in the deep crust to explain the formation of uniform tonalitic melts at shallower crustal levels in the BVIS. This process also explains the unusual predominance of orthopyroxene in the BVIS, and the limited aluminum enrichment compared to experimental differentiation sequences of hydrous basalts. Considering the similar geochemical characteristics of intermediate and felsic igneous rocks from the Sierra Nevada batholith and the Cascades, mixing magmas of variable H₂O contents in the lower crust represents a viable petrological process to produce SiO₂-rich liquids that may be more common than previously recognized.

Keywords: Sierra Nevada batholith, Arc magmas, Crystallization-differentiation, Magma mixing, Lower continental crust.

1. Introduction

The formation of continental crust results from igneous processes forming large batholiths and volcanic provinces in subduction zones (Jagoutz and Schmidt 2012; Rudnick and Fountain 1995; Taylor and McLennan 1995). Yet, the dominant mechanisms responsible for generating andesitic continental crust remains actively debated. A popular model whereby partial re-melting of lower crustal lithologies produces silica-rich igneous rocks via dehydration reactions has been experimentally reproduced and is supported by migmatitic fabrics and supracrustal-derived isotopic composition (Clemens et al. 2011; Clemens and Stevens 2012; Davidson and Arculus 2005; Patiño Douce 1995; Rapp and Watson 1995; Roberts and Clemens 1993; White and Chappell 1983). In contrast, compelling evidence collected from field and experimental studies challenge this view and suggest that primitive arc melts crystallizing lower crustal ultramafic and mafic cumulates produce intermediate to silica-rich magmas similar to continental crust (Bucholz et al. 2014a,b; Dessimoz et al. 2012; Guo et al. 2020; Jagoutz 2010; Jagoutz and Klein 2018; Melekhova et al. 2015; Müntener and Ulmer 2018; Nandedkar et al. 2014; Tuttle and Bowen 1958; Ulmer et al. 2018). In this model, delamination of the dense mafic component would explain the relatively low volume of preserved mafic material and the andesitic bulk composition of the continental crust (Arndt and Goldstein 1989; Jagoutz and Behn 2013; Jagoutz and Kelemen 2015; Jull and Kelemen 2001; Kay and Kay 1993), migmatite-like textures result from the deformation of partially crystallized magma (Sawyer 2000), and isotopic variations in felsic rocks fingerprint variable extents of crustal assimilation (De Paolo 1981; Hildreth and Moorbath 1988; Jagoutz and Klein 2018). A final proposed deep crustal mechanism to produce differentiated arc magmas is magma mixing between primitive arc basalts and highly evolved felsic melts likely generated by incipient melting of pre-existing gabbroic crust (Blatter et al. 2013, 2017).

As either model predicts important processes related to crustal differentiation occurring in the lower arc crust through melting, assimilation, storage and homogenization (MASH or hot zone; Annen et al. 2006; Hildreth and Moorbath 1988; Jagoutz 2014), direct assessments of the aforementioned mechanisms are limited to few tectonically exposed arc lower crustal sections. Among them, the predominant role of crystallization-differentiation has been unequivocally demonstrated in the Kohistan arc (Jagoutz et al. 2009, 2011; Jagoutz 2010), the Talkeetna arc (Greene et al. 2006; Hacker et al. 2008), the Chelan complex in the Cascades (Dessimoz et al. 2012), the Dariv complex in Western Mongolia (Bucholz et al. 2014a,b), the Famatina arc (Otamendi et al. 2012; Walker et al. 2015) and the Gangdese arc (Guo et al. 2020). In contrast, magmatic processes accounting for the genesis of intermediate to felsic magmas in the Sierra Nevada batholith (SNB) remains equivocal between petrogenetic models suggesting partial melting of pre-existing lower crustal lithologies in the MASH zone, fractional crystallization and assimilation of crustal material in the deep or shallow crust, mixing of primitive basalt with highly

differentiated melt, or a combination of all of these mechanisms (Blatter et al. 2013; Ducea and Saleeby 1998; Klein et al. 2021; Klein and Jagoutz 2021; Lackey et al. 2005; Nadin and Saleeby 2008; Pickett and Saleeby 1993, 1994; Ratajeski et al. 2005; Saleeby et al. 1987, 2003, 2007, 2008; Sisson et al. 2005).

This study evaluates the deep magmatic processes recorded by the formation of lower crustal mafic igneous cumulates (8-9 kbars) and shallower felsic plutonic rocks (3-7 kbars) in the Bear Valley intrusive suite (BVIS), which represents a ~25-30 km thick continuous crustal arc section emplaced within 1.39 Myr in the southern SNB (Fig. 1; Klein et al. 2021; Klein and Jagoutz 2021; Nadin and Saleeby 2008; Pickett and Saleeby 1993, 1994; Ross 1989; Saleeby et al. 1987, 2007, 2008). Here, we present petrography and mineral chemistry to constrain the sequence of mineral crystallization, the parental melt compositions and the pressures and temperatures of crystallization. We show that gabbros crystallized from parental melts with distinct compositions and H₂O contents. We also calculate the trace element composition of a parental melt in equilibrium with the igneous mafic cumulates and show that this composition is comparable to the felsic liquids emplaced at shallower crustal levels. We then compute mixing models of variably fractionated dry and wet basalts in the lower crust that enable us to explain geochemical characteristics of differentiated melts and the unusual predominance of orthopyroxene in the BVIS.

2. Geological setting

The SNB is one of the largest batholiths exposed within the North America Cordillera, extending over ~600 km along NNW strike and a width varying between ~80 and 120 km (Fig. 1a). The SNB records successive magmatic pulses in the Triassic (200-250 Ma), Jurassic (145-165 Ma), and Cretaceous (85-120 Ma), but the majority of the exposed SNB is composed of arc-related intermediate to felsic intrusions primarily formed in the Cretaceous (Chen and Moore 1982; Coleman and Glazner 1997; Ducea 2001; Ducea and Barton 2007; Paterson and Ducea 2015) as a result of subduction of the Farallon plate (Ducea 2001; Glazner 1991; Saleeby et al. 2003). Ultramafic xenoliths in Miocene-Quaternary lavas overlying Late Cretaceous granitoids in the central SNB indicate a crustal thickness of ~40-50 km (Dodge et al. 1986; Ducea and Saleeby 1998; Lee et al. 2006), consistent with a crustal thickness of ~30-55 km determined from seismic studies (Das and Nolet 1998; Flidner et al. 2000; Mooney and Weaver 1989; Ruppert et al. 1998; Wernicke et al. 1996).

The northern and central SNB expose plutons dominantly emplaced in the upper to middle crust with emplacement pressures of 2-4 kbars (~6-12 km depth). In contrast, the southern SNB is characterized by a gradient in emplacement pressure increasing from 3-4 kbars in the north to 8-9 kbars in the south (Ague 1997; Dixon 1995; Chapman et al. 2012; Klein and Jagoutz 2021; Nadin and Saleeby 2008; Pickett and Saleeby 1993; Ross 1985, 1987, 1989; Saleeby et al. 1987, 2003, 2007). The tilting and exhumation of lower crust (~8-9 kbars) in the southernmost SNB is thought to result from shortening and extensional deformation associated with Late Cretaceous flat subduction of the Farallon slab in this region (Ducea and Saleeby 1998; Saleeby et al. 2003). During this period, the shallow slab subduction mechanically removed the high-density batholithic root beneath the southern SNB, leading to gravitational collapse at ~80-90 Ma (Chapman et al. 2012; Saleeby et al. 2003, 2008). Vertical displacement and horizontal shortening of the

regional primary batholithic structure is recorded by the complex structural evolution of the proto-Kern Canyon fault in its central part (Fig. 1a; Glazner 1991; Malin et al. 1995; Nadin and Saleeby 2008; Nadin et al. 2016; Saleeby et al. 2003, 2008; Wood and Saleeby 1997).

3. The Bear Valley Intrusive Suite

The Bear Valley Intrusive Suite (BVIS) extends for over ~60 km in the southernmost SNB, with pressures of formation of ~8-9 kbars in the south to ~3-4 kbars in the north, representing a ~30 km-thick continuous exposed crustal section (Fig. 1b; Pickett and Saleeby 1993). The BVIS intruded the 120-115 Ma Tehachapi Gneiss Complex and metasedimentary units that crop out as structurally coherent metamorphic pendants throughout the southern SNB (Fig. 1; Nadin and Saleeby 2008; Ross 1989; Saleeby et al. 2003). Recent high-precision U-Pb zircon geochronology indicates that the majority of the BVIS was rapidly emplaced within 1.39 ± 0.06 Myr between 100.06 ± 0.02 Ma and 101.45 ± 0.06 Ma (Klein et al. 2021), consistent with previous lower precision laser ablation ICP-MS and multi-grain TIMS zircon geochronology (Pickett and Saleeby 1994; Saleeby et al. 1987, 2007; Sams 1986). Most of the northern part of the BVIS consists of the hypersthene-free Tonalite of Bear Valley Springs emplaced at ~2-6 kbars, along with the smaller Poso Flat granodiorite and Tonalite of Mount Adelaide (Fig. 1b; Ague 1997; Nadin and Saleeby 2008; Ross 1989; Pickett and Saleeby 1993). To the south, the Tonalite of Bear Valley Springs transitions to the hypersthene-bearing Tonalite of Bison Peak, which was emplaced at ~6-7 kbars (Fig. 1b). This unit is in contact with the Tehachapi Gneiss Complex to the west and south, and proximal to the Garlock fault zone to the east. Further to the southwest and at increasing emplacement pressures, the hornblende-bearing Tunis Creek gabbros crop out as isolated bodies within the Tehachapi Gneiss Complex (Fig. 1b). The Tunis Creek gabbros expose a variety of coarse- to medium-grained (2 mm to >5 cm), weakly to non-foliated mafic intrusions dominated by plagioclase, orthopyroxene, and amphibole, and comparatively rare olivine and clinopyroxene (Pickett and Saleeby 1993; Sams 1986; this study). Subsidiary ultramafic stocks occur further south in Pastoria Creek, together with garnet-bearing gabbros and tonalites in Grapevine Canyon (Fig. 1b; Pickett and Saleeby 1993, 1994; Ross 1989; Sams 1986). The lithologies investigated in this study include Tunis Creek gabbros, hypersthene-bearing Tonalite of Bison Peak (hereafter referred as BPT) and hypersthene-free Tonalite of Bear Valley Springs (BVST), representing a structurally coherent crustal section of spatially and temporally-related intrusions. Based on petrography and mineral chemistry, we subdivided the Tunis Creek gabbros into six types: olivine metagabbro and metatroctolite enclave (hereafter referred as TCG1), olivine-hornblende orthopyroxenite (TCG2), olivine-hornblende norite (TCG3), hornblende norite (TCG4), hornblende gabbro-norite (TCG5) and hornblendite-hornblende gabbro (TCG6). Petrographic characteristics based on 55 petrographic thin sections of plutonic rock samples are summarized in Table 1 and illustrated in Figure 2, while phase proportions expressed as volume percent based on visual estimates are reported in Supplementary Data Table S1.

4. Analytical methods

Electron microprobe analyses

The major element compositions of major mineral phases ([Supplementary Data Table S2](#)) were determined using a JEOL JXA-8200 Superprobe electron probe micro-analyzer at the Department of Earth, Atmospheric and Planetary Sciences at Massachusetts Institute of Technology, Cambridge, MA, USA. Natural and synthetic silicate and oxide phases were used as standards. The measurement operating conditions were an accelerating voltage of 15 kV and a beam current of 10 nA. Depending on the nature of the analyzed elements (i.e., alkali and non-alkali), counting times were 10s–60s on peak ($K\alpha$) and 5s–30s on the respective background. The typical standard deviation of counts on individual analyses was between 0.5 and 1%. The raw data were corrected for matrix effects with the CITZAF package ([Armstrong 1995](#)).

LA-ICP-MS trace element analyses

In situ trace element compositions of plagioclase, pyroxene, and amphibole phases were obtained at Rutgers University using a Thermo Scientific iCAP Qc inductively coupled plasma mass spectrometry (ICP-MS) system equipped with a Photon Machines 193 nm laser ablation system. Spot sizes of 65 μm were used for plagioclase, and 40 μm spot sizes were used for pyroxene and amphibole. Approximately 10 s of gas background was collected before 30 s of sample ablation. Standards NIST610 and NIST612 were regularly analyzed for continuous calibration and to account for any drift. BCR and BIR were also analyzed regularly as a secondary standard to confirm accuracy ([Supplementary Data Table S3](#)). Raw data were processed off-line using an “in-house” procedure and averages of 30 s signal intervals were manually set to yield a representative signal and to avoid contamination from mineral inclusions. Electron microprobe data were used as an internal standard for all analyzed minerals, using Ca for plagioclase and Si for pyroxene and amphibole.

5. Mineral chemistry

Major and trace element mineral compositions of olivine, orthopyroxene, clinopyroxene, amphibole and plagioclase are presented in [Supplementary Data Tables S2 and S3](#). The range in Mg# (molar $\text{Mg}/(\text{Mg}+\text{Fe}_{\text{tot}})$) of olivine, orthopyroxene, clinopyroxene and amphibole, and in anorthite content (An) of plagioclase are summarized in [Figure 3](#) while detailed mineral major and trace element compositions are shown in [Figures 4-6](#).

Olivine

Olivine in TCG1 have Mg# ranging from 0.68 to 0.75 ([Fig. 3](#)). Olivine in TCG2 and TCG3 have similar Mg# of 0.73-0.74 and 0.68-0.69, respectively ([Fig. 3](#)). The Ni content of olivine in all these rocks is low ≤ 500 ppm. The low Mg# and Ni content indicate that olivine did not crystallize from a primitive mantle melt.

Orthopyroxene

Primary orthopyroxene phenocrysts compositions in TCG2-5 and BP range from bronzite to hypersthene. Orthopyroxene in TCG2 have the highest observed Mg# of 0.72-0.76 and Al_2O_3 contents of 2.4-3 wt. %, while TCG3 display slightly lower Mg# of 0.68-0.7 and Al_2O_3 contents of 1.5-2.9 wt. % ([Fig. 3 and 4a](#)). Orthopyroxene crystallized in TCG4 is characterized by lower Mg# and Al_2O_3 ranging from 0.5 to 0.64 and from 0.9 to 1.7 wt. %, respectively ([Fig. 4a](#)). The positive correlation between Mg# and Al_2O_3 content of

orthopyroxene in TCG2, TCG3 and TCG4 mimics melt differentiation trends in ultramafic-mafic lower crustal cumulates of the Chilas complex in the Kohistan arc (Jagoutz *et al.* 2007), the Talkeetna Arc (DeBari and Coleman 1989; Greene *et al.* 2006) and in the Sierra Vallee F  rtil in the Famatina arc (Walker *et al.* 2015). Orthopyroxene in TCG5 displays Mg# of 0.67-0.72 and substantially lower Al₂O₃ values of 0.6-1.1 wt. % (Fig. 4a). Relict orthopyroxene in BPT have Mg# of 0.51-0.54 and Al₂O₃ of 1.1-1.5 wt. % overlapping in composition with the most evolved orthopyroxene crystallized in TCG4 (Fig. 4a). Although CaO contents overlap between individual samples, average CaO contents of orthopyroxene in TCG5 (0.58-0.64 wt. %) are higher than orthopyroxene in TCG2, TCG3 and TCG4 (0.24-0.51 wt. %), and are similar to BP (0.64-0.65 wt. %). However, orthopyroxenes in all Tunis Creek gabbros (TCG2-5) display significantly lower MnO contents (0.3-0.6 wt. %) compared to orthopyroxene in BP (1 -1.3 wt. %). The TiO₂ contents are comparably low among all primary orthopyroxenes at <0.1 wt. %.

Orthopyroxene crystallized in the multi-layered corona reactions around olivine are dominant in TCG1 (Fig. 2a,b), whereas this texture is cryptic in TCG3. Coronal orthopyroxenes are characterized by high Mg# ranging from 0.73-0.77 and highly variable Al₂O₃ content (0.7-2.7 wt. %) (Fig. 4a). Other elements (CaO, MnO, TiO₂,) are highly variable and overlap with primary orthopyroxene compositions.

The primitive mantle normalized trace element compositions (McDonough and Sun 1995) of primary orthopyroxene in TCG4 and TCG5 are characterized by similar trace element patterns with light rare earth element (LREE), Sr and Zr depletions (Fig. 6a). The trace element pattern of orthopyroxene remnants in BP mostly overlap with those crystallized in Tunis Creek gabbros but tend to exhibit a marked enrichment in heavy rare earth element (HREE) with respect to middle and light rare earth elements (MREE and LREE) (Fig. 6a). Except for a few elements (Th, La, Ce, Pr, Y), the trace element composition of orthopyroxene in corona textures in TCG1 is barely detectable (Fig. 6a).

Clinopyroxene

Clinopyroxene in TCG1 occurs as phenocrysts and plagioclase-hosted inclusions, both of which are characterized by Mg# of 0.84-0.86 (Fig. 3). Phenocrysts display higher Al₂O₃ (2.3-2.6 wt. %) compared to plagioclase-hosted inclusions that have lower Al₂O₃ (0.9-1.8 wt. %) (Fig. 4b), where lower Al₂O₃ contents are interpreted to reflect co-crystallization of plagioclase. Clinopyroxene in TCG5 displays lower Mg# of 0.78-0.83 than those crystallized in TCG1 and Al₂O₃ (0.8-2 wt. %) contents overlapping with plagioclase-hosted inclusions in TCG1 (Fig. 4b). The range of Mg# for clinopyroxene in TCG1 and TCG5 overlaps with those crystallized in ultramafic rocks and gabbro-norite in the Chilas complex in the Kohistan arc (Jagoutz *et al.* 2007), the Talkeetna Arc (DeBari and Coleman 1989; Greene *et al.* 2006) and the Sierra Valle F  rtil in the Famatina arc (Walker *et al.* 2015), although the Al₂O₃ content for clinopyroxene in the BVIS is systematically lower (Fig. 4b). Remnants of clinopyroxene in BPT are characterized by significantly lower Mg# of 0.66 combined with a range of Al₂O₃ contents (1.6-2.2 wt. %) that overlap with clinopyroxene crystallized in Tunis Creek gabbros. Clinopyroxene phenocrysts crystallized in TCG1 display higher TiO₂ (0.2-0.5 wt. %) and Cr₂O₃ (0.1-0.2 wt. %) contents compared to plagioclase-hosted inclusions that have lower TiO₂ (0.1-0.2 wt. %) and Cr₂O₃ contents (<0.02 wt. %). Clinopyroxene in TCG5

and BPT have overlapping compositions characterized by TiO_2 of 0.1-0.3 wt. % and Cr_2O_3 up to 0.2 wt. %. From TCG1 to TCG5 and BPT, we observe a progressive decrease in CaO contents combined with a progressive increase of Na_2O contents in clinopyroxene.

The normalized trace element patterns of clinopyroxene in TCG5 show depletion of large-ion lithophile elements (LILE) and high-field-strength elements (HFSE) with respect to LREE, MREE, and HREE (Fig. 6b). In BPT, the absolute clinopyroxene trace elements compositions are elevated relative to those in hornblende gabbro and display a flat REE pattern (Fig. 6b). For both rock types, the pronounced Eu negative anomalies of 0.3-0.5 ($Eu_N/\sqrt{Sm_N * Gd_N}$) and depletion in Sr, Zr and Hf suggest clinopyroxene crystallization from a parental melt saturated in plagioclase and zircon. The trace element compositions of clinopyroxene in TCG1 could not be accurately determined due to the abundance of Fe-Ti exsolution trails in clinopyroxene phenocrysts and the small size of plagioclase-hosted clinopyroxene inclusions (15-20 μm).

Amphibole

Primary amphiboles are tschermakite, hastingsite, and magnesio-hornblende (based on the classification scheme of Leake et al., 1997; Fig. 5a). Amphibole in TCG2 and TCG3 display the highest Mg# of 0.69-0.79 with low Si contents of 6.1-6.4 a.p.f.u, whereas TCG4 and TCG6 overlap in compositions and exhibit large range of lower Mg# of 0.49-0.71, and Si contents of 6-6.8 a.p.f.u (Fig. 5a). In contrast, amphibole in TCG5 has restricted high Mg# of 0.73-0.81 and higher Si contents of 6.7-7.2 a.p.f.u (Fig. 5a). Within the tonalites, amphiboles in BPT are characterized by low Mg# of 0.47-0.52 and Si content of 6.1-6.3 a.p.f.u compared to amphibole in BVST characterized by a wide range of Mg# of 0.4-0.72 and Si content of 6.3-7.5 a.p.f.u (Fig. 5a). Amphibole in TCG2, TCG3, TCG6 (hornblende), and BPT have elevated $(\text{Na}+\text{K})_A$ contents of 0.4-0.6 a.p.f.u, compared to other samples that contain amphibole with a lower range of $(\text{Na}+\text{K})_A$ contents of 0.1-0.4 a.p.f.u (Fig. 5b). In TCG2, TCG3, TCG4 and TCG6, amphiboles display on average higher Al^{IV} (1.5-1.9 a.p.f.u) and Al^{VI} (0.4-0.7 a.p.f.u) and a wide range of Ca_B (1.4-1.8 a.p.f.u) contents compared to amphibole in TCG5 and BVST (Al^{IV} of 0.8-1.5 a.p.f.u, Al^{VI} of 0.1-0.4 a.p.f.u, Ca_B of 1.7-1.9 a.p.f.u) (Fig. 5b-d). Amphibole in BPT display high Al^{IV} of 1.7-1.9 a.p.f.u and Ca_B of 1.7-1.8 a.p.f.u combined with intermediate Al^{VI} of 0.4 a.p.f.u contents (Fig. 5b-d). Amphibole crystallized in multi-layered corona in TCG1 are restricted to tschermakite (Fig. 5a) and are characterized by high Mg#, $(\text{Na}+\text{K})_A$, Al^{IV} , Al^{VI} and Ca_B together with low Si contents (Fig. 5a-d).

The broad positive correlations between $(\text{Na} + \text{K})_A$ versus Al^{IV} within and between samples indicate the extent of the temperature-sensitive edenite exchange (Fig. 5b). While the pressure-sensitive Al-Tschermak exchange is poorly correlated for Tunis Creek gabbros, the positive correlation observed for BVST suggests a pressure control consistent with the wide range of pressure estimates for these samples (Fig. 5c, Table 2). The broad correlation between Ca_B and Al^{IV} indicates the influence of plagioclase co-crystallization for most Tunis Creek gabbros (Fig. 5d). In contrast, amphibole in TCG5 and tonalites display no correlation, which suggest limited plagioclase co-crystallization. In this case, plagioclase

crystallization before amphibole is consistent with the petrography and the trace element chemistry described below.

The normalized amphibole trace element patterns in Tunis Creek gabbros significantly overlap with little variation in absolute concentrations between samples (Fig. 6c). Trace element patterns are characterized by depletions in HFSE, and LILE and in LREE with respect to MREE and HREE. Amphibole Eu anomalies are either absent or negative ranging from 0.6 to 0.8 in TCG4, from 0.7 to 1 in TCG6 and from 0.4 to 0.5 in TCG5 (Fig. 6c). This indicates the predominance of plagioclase crystallization prior to or co-crystallizing with amphibole. In contrast, the normalized trace element pattern for amphibole crystallized in multi-layered corona textures for TCG1 shows enrichment in HFSE and LREE with respect to MREE and HREE combined with significant positive Eu anomalies of 1.3-3.1 indicative of subsolidus reactions further discussed in section 7.1 (Fig. 6c). Amphibole in BPT is enriched in trace elements compared to Tunis Creek Gabbros, with marked Eu negative anomalies of 0.4-0.5 (Fig. 6c) consistent with crystallization from a differentiated parental melt saturated in plagioclase.

Plagioclase

The highest and fairly restricted plagioclase An contents are found in TCG1 (An₈₈₋₉₈) and in TCG3 (An₈₆₋₉₇). Slightly lower values are observed in TCG4 (An₇₁₋₈₇) and in TCG5 (An₇₇₋₉₀). Finally, heterogeneous An contents extending to much lower values are found in TCG6 (An₅₀₋₉₂), and in BPT and BVST (An₃₁₋₆₀) (Fig. 3). Zoning in plagioclase crystals is restricted to rare normally zoned thin rims with An₄₈₋₆₁ in TCG5, and rare resorbed sieve-textured cores with An₇₁₋₇₂ in BVST (Fig. 3). A general observation is that An contents decrease from Tunis Creek gabbros to BPT and BVST (Fig. 3). A similar trend is observed with the increase of K₂O concentration from <0.05 wt. % in plagioclase in Tunis Creek gabbros up to 0.5 wt. % in plagioclase in BPT and BVST. The large range of An contents between and within the same rock types suggests plagioclase crystallization in equilibrium with evolving melt compositions.

The normalized trace element patterns are almost identical for plagioclase in TCG4, TCG5 and TCG6 (Fig. 6d). Trace element patterns for plagioclase in TCG1 are characterized by the lowest observed LREE content. The highest LREE and LILE contents are observed in plagioclase in BPT indicative of crystallization from a fractionated melt compared to Tunis Creek gabbros (Fig. 6d).

Oxides

Spinel symplectites occur in TCG1 and TCG3 ranging in composition from pleonaste to hercynite (Supplementary Data Table S2). Chromite is also present in the multi-layers corona texture of TCG1. Sparse analyses of oxides indicate ilmenite is the dominant oxide both in Tunis Creek gabbros and in BPT and BVST with rare magnetite (Supplementary Data Table S2).

6. Bulk rock geochemistry

Major and trace element whole rock analyses are presented in Klein and Jagoutz (2021). Here, we present the same dataset in Figures 7 and 8 to highlight the different rock types of Tunis Creek gabbro described above. The whole rock Mg# (molar Mg/(Mg+Fe) considering all Fe as FeO) for Tunis Creek gabbros varies from 0.73 to 0.44 and SiO₂ contents vary from 43 to 51 wt. % (Fig. 7a). Olivine-bearing gabbros (TCG1,2

and 3) and hornblende gabbro (TCG5) exhibit a narrow range of the highest observed whole rock Mg#. In contrast, hornblende norite (TCG4) and hornblende gabbro (TCG6) are characterized by a wide range of whole rock Mg# (Fig. 7) correlating with the wide variations of Mg# in orthopyroxene and/or amphibole in these rock types (Figs. 4 and 5). Tonalites are characterized by low Mg# of 0.55-0.37 and higher SiO₂ contents of ~56-67 wt. % (Fig. 7a). The K₂O contents are lowest in Tunis Creek gabbros (<0.05-0.2 wt. %) and increases in tonalites (1.2-3.3 wt. %) illustrating the incompatible character of K₂O during melt differentiation (Fig. 7b). The TiO₂ concentrations in Tunis Creek gabbros vary from 0.1 to 2.2 wt.% and is negatively correlated with SiO₂. The highest TiO₂ values are measured in TCG6 indicative of Fe-Ti-oxides and amphibole accumulation (Fig. 7c). Tonalites display a gentle negative correlation of TiO₂ (0.61-1.02 wt. %) with SiO₂ (Fig. 7c), suggestive of melt fractionation by progressive crystallization of amphibole, Fe-Ti oxides, and biotite. Most of the Tunis Creek gabbros are characterized by Al₂O₃ contents between 15-25 wt. % (Fig. 7d). Significantly lower concentrations of 7.6-9.4 wt. % Al₂O₃ in TCG2 and TCG5 reflect the predominance of pyroxenes relative to plagioclase, and are consistent with TCG2 containing the lowest observed CaO contents, reflecting the absence of plagioclase. Al₂O₃ contents in tonalites show limited variation between ~15 and 19 wt. % (Fig. 7d). The Na₂O content is positively correlated with SiO₂, similar to K₂O (Fig. 7e), while CaO, FeO_{tot} and MgO content are negatively correlated with SiO₂ (Fig. 7f,g) consistent with continuous fractionation of ferro-magnesian minerals and plagioclase. Most samples have Ni contents <50 ppm, with few samples up to ~150 ppm, and most samples have Cr contents <100 ppm, with few samples up to ~360 ppm.

Primitive mantle normalized (McDonough and Sun 1995) trace element patterns for Tunis Creek gabbros are characterized by a progressive increase in absolute concentrations that correlates with decreasing Mg# and hence differentiation (Fig. 8a,b). The overall trace element pattern is characterized by flat to depleted HFSE, LILE and LREE with respect to MREE and HREE. The majority of Tunis Creek gabbros display positive Sr, Eu (>0.9-2.2), Pb and Ti anomalies (except for one hornblende gabbro; Figs. 7h and 8a), consistent with plagioclase accumulation. Only TCG5 shows marked negative Eu, Pb and Ti anomalies combined with no Sr positive anomaly, consistent with crystallization from a melt that experienced extensive plagioclase and Fe-Ti oxides fractionation (Figs. 7h and 8a). TCG1 is characterized by the lowest MREE and HREE abundances. In contrast, TCG6 samples are characterized by a progressive increase in REE absolute concentrations with decreasing Mg#. This increase is associated with reduced Ti and Nb negative anomalies, consistent with an increase in amphibole/melt D_{Nb}, D_{Ti} and D_{Nb/Ta} upon magma cooling and crystallization (Li et al. 2017; Nandedkhar et al. 2016). Tonalite trace element patterns compared to Tunis Creek gabbros show significant enrichments in LILE, HFSE and LREE with similar to slightly enriched HREE (Fig. 8c). The trace element patterns for BP and BVST show marked Eu, Sr and Ti negative anomalies, as well as positive Zr and Hf anomalies that are consistent with a zircon-saturated differentiated melt (Figs. 7h and 8c).

7. Discussion

7.1 Evidence for subsolidus reactions

Petrographic and geochemical evidence support the evolution of the BVIS primarily controlled by igneous processes. However, microtextural observations and mineral chemistry indicate post-emplacement, subsolidus processes under amphibolite-granulite facies conditions. Exsolution lamellae in orthopyroxenes typically reflect subsolidus re-equilibration during slow cooling. This textural evidence is correlated by a slight negative correlation between Al_2O_3 and Mg# ascribed to a metamorphic trend due to Tschermak exchange $(\text{Fe, Mg})\text{SiAl}_2$ during cooling (Fig. 4a; Jagoutz et al. 2007). Furthermore, amphibole compositions are characterized by a positive correlation of Mg# and Si p.f.u within a given sample indicative of subsolidus re-equilibration (Fig. 5a; Dessimoz et al. 2012). In TCG1, we observe well-developed multi-layered corona textures consisting of orthopyroxene, amphibole, and amphibole + spinel (\pm clinopyroxene) symplectite from cumulus olivine to plagioclase (Fig. 2b). Corona textures with or without the presence of amphibole are frequently observed in ultramafic-mafic gabbros at amphibolite-granulite conditions (e.g., Helmy et al. 2008; Jagoutz et al. 2007; Otamendi et al. 2010). In the absence of amphibole, anhydrous corona textures are formed by metamorphic solid-state reaction between plagioclase and olivine (Gallien et al. 2012; Jagoutz et al. 2007; Kushiro and Yoder 1966). In contrast, hydrous corona textures are often interpreted to reflect crystallization of an intercumulus hydrous melt and/or fluids (de Haas et al. 2002; Gallien et al. 2012; Helmy et al. 2008; Otamendi et al. 2010), although diffusion-controlled reaction kinetics (Joesten 1986) and solid-state reactions (Ashworth 1986) have also been proposed. In the BVIS, the orthopyroxene composition in coronas differs from primary orthopyroxene, with lower trace element contents and a pronounced negative correlation between Mg# and Al_2O_3 (Figs. 4a and 6a). This difference is consistent with growth of coronal orthopyroxene at the expense of trace element-poor olivine together with subsolidus re-equilibration upon cooling following the solid-state reaction: $\text{olivine} + \text{plagioclase} \rightarrow \text{orthopyroxene} + \text{spinel} \pm \text{clinopyroxene}$. The normalized trace element patterns of coronal amphibole show enrichment in HFSE and LREE, depletion in MREE and HREE, and marked positive Eu anomalies of 1.3-3.1 compared to primary amphiboles (Fig. 6d). These geochemical features suggest formation of coronal amphibole at the expense of plagioclase following the fluid-driven reaction: $\text{plagioclase} + \text{orthopyroxene} + \text{H}_2\text{O} (\pm \text{clinopyroxene}) \rightarrow \text{amphibole} + \text{spinel}$. Although the exact mechanisms for forming the multi-layered corona textures found in the BVIS are beyond this paper's scope, it seems to primarily result from subsolidus solid-state reactions, where the formation of amphibole requires the presence of H_2O for which magmatic or metamorphic origins are possible.

7.2 Mineral chemistry and the crystallization sequences recorded in Tunis Creek gabbros

The whole rock geochemistry and mineral assemblages of Tunis Creek gabbros reflect the accumulation of ferro-magnesian phases, plagioclase, and oxides in variable proportions consistent with formation as igneous cumulates. Excluding TCG1 which is affected by important sub-solidus re-equilibration, TCG2 and TCG3 are the most primitive rocks observed in the BVIS with preserved cumulates textures (Fig. 2c,d). In these samples, olivine and orthopyroxene with similar Mg# suggest co-crystallization assuming a similar $Kd^{\text{Fe-Mg}}$ of ~ 0.3 (Beattie 1993; Roeder and Emslie 1970), although the resorbed olivine crystals likely

crystallized as the earliest phase. Based on the absence of plagioclase and the crystallization of large amphibole oikocrysts in TCG2, we propose the following sequence of mineral crystallization: olivine → orthopyroxene → amphibole. In contrast to TCG2, in TCG3 orthopyroxene, plagioclase and amphibole each contain inclusions of the other two phases indicative of the following sequence of mineral crystallization: olivine → orthopyroxene + amphibole + plagioclase. Lower Mg# and Al₂O₃ content in orthopyroxene for TCG3 could be explained by crystallization from a more differentiated melt and the appearance of plagioclase. Furthermore, the coexistence of low Fo₆₈₋₇₄ olivine and high An₈₆₋₉₇ plagioclase in TCG2 requires H₂O-rich melts (Tollan et al. 2012), which is consistent with the olivine-orthopyroxene-amphibole mineral assemblage in TCG3 (e.g., Melekhova et al. 2015) and the large amphibole oikocrysts in both TCG2 and TCG3. Hence, we argue that TCG2 and TCG3 crystallized from the same hydrous parental melt at different stages along one liquid line of descent.

The progressive decrease of low Mg# and low Al₂O₃ concentrations in orthopyroxenes in TCG4 clearly indicates plagioclase co-crystallization as the parental melt fractionates (Fig. 4a). This is also consistent with plagioclase inclusions in orthopyroxene. Interstitial amphiboles are characterized by negative Eu anomalies indicative of late crystallization with respect to plagioclase and orthopyroxene. In TCG5, the low Al content and marked negative Eu anomalies in pyroxene and amphibole reflect plagioclase crystallization prior to and/or co-crystallizing with pyroxenes and amphiboles. Moreover, resorbed pyroxenes in amphibole indicate the late crystallization of amphibole with respect to other phases. Collectively, our textural observations and chemical data for TCG4 and TCG5 suggest a crystallization sequence of plagioclase + orthopyroxene (± clinopyroxene) → amphibole. However, orthopyroxene and amphibole compositions differ significantly between TCG4 and TCG5 and indicate crystallization from distinct parental melts (Figs. 4a and 5). The late appearance of interstitial amphibole also suggests drier parental melts than the ones crystallizing TCG2 and TCG3.

In TCG6, absent to negative Eu anomalies in amphibole combined with a positive correlation ($r^2=0.8$) between amphibole Mg# and plagioclase An content indicates amphibole crystallization prior to and/or co-crystallizing with plagioclase. This is also consistent with intercumulus plagioclase textures (5-10%) in hornblendite indicative of early amphibole crystallization. The observation of rare pyroxene remnants in amphibole suggest a sequence of crystallization of pyroxene → amphibole → plagioclase. The early crystallization of amphibole relative to plagioclase contrasts with the late crystallization of amphibole in TCG4 and TCG5, which ultimately argues for the crystallization of TCG6 from an H₂O-rich parental melt (Krawczynski et al. 2012).

Finally, the magmatic mineralogy of TCG1 consists of olivine, clinopyroxene and plagioclase, where clinopyroxene inclusions in plagioclase suggests the following sequence of crystallization: olivine + clinopyroxene → plagioclase. While the coexistence of low Fo olivine and high An plagioclase requires crystallization from a H₂O-rich melts, the absence of primary orthopyroxene and amphibole in TCG1 argues for a distinct parental melt composition compared to the other Tunis Creek gabbros. To summarize, the contrasting sequence of mineral crystallization and mineral chemistry observed for spatially and

temporally related Tunis Creek mafic gabbros (Klein and Jagoutz 2021; Klein et al. 2021) suggests the contemporaneous differentiation of parental melts with different compositions and water contents in the lower crust of the Sierran arc.

7.3 Intensive variables

Pressure estimates

Emplacement pressures in the BVIS were estimated by Klein and Jagoutz (2021) from interpolated pressure surface following the methods of Nadin and Saleeby (2008) and Chapman et al. (2012). Using this interpolation method, the samples examined here have estimated emplacement pressures of 8.3-8.4 kbars for Tunis Creek gabbros, 6.3-6.7 kbars for BPT, and 3.4-6 kbars for BVST (Table 2). Using Al-in-hornblende geobarometer (e.g., Schmidt 1992) in tonalites that crystallize the appropriate mineral assemblage buffer (amphibole - biotite - plagioclase - orthoclase - quartz - sphene - Fe-Ti-oxides), we calculate pressure estimates of 7.2-7.3 kbars for BPT and of 2.3-6.6 kbars for BVST (Table 2). Two-pyroxenes barometer of Putirka (2008, eq. 39) applied to hornblende gabbro-norite in Tunis Creek (TCG5) yields pressure estimates of 9.4-11.0 kbars (± 3.7) (Table 2). Overall, the range of new calculated pressure from mineral chemistry is consistent with interpolated pressures calculated by Klein and Jagoutz (2021).

Temperature estimates

We calculated crystallization temperatures using amphibole-plagioclase (Holland and Blundy 1994; uncertainty of $\pm 40^\circ\text{C}$; hereafter referred as HB94) and hornblende-only geothermometers (Putirka 2016; uncertainty of $\pm 30^\circ\text{C}$; hereafter referred as P16) (Table 2). Although the calculated temperatures using both methods show very similar patterns (Fig. 9), amphibole crystallization temperatures calculated using P16 are lower for Tunis Creek gabbros and higher for tonalites compared to HB94. The higher crystallization temperatures in the Tunis Creek gabbros (HB94: 810-1070°C vs. P16: 790-945°C) tends to be more consistent with amphibole bearing experiments conducted at lower crustal pressure (Blatter et al. 2013; Melekhova et al. 2015; Nandedkar et al. 2014; Ulmer et al. 2018). For this reason, we focus on temperature estimates for amphibole crystallization based on HB94.

The calculated crystallization temperatures for amphibole in TCG3 are $\sim 1055 \pm 55^\circ\text{C}$, whereas the absence of plagioclase in TCG2 precludes using HB94 to estimate temperature. However, the positive correlation between P16 and HB94 and similar temperature estimates between TCG2 and TCG3 using P16 strongly suggests similar high temperature for amphibole crystallization in TCG2. Complementary estimates of olivine liquidus temperatures in TCG2 and TCG3 range from ~ 1070 - 1110°C (Table 2) based on anhydrous conditions calculation (Niu et al. 2002) corrected for the effect of pressure (Herzberg and O'Hara 2002) and of H_2O (Médard and Grove 2008) assuming 2-3 wt. % H_2O further discussed in the next section. Collectively, this indicates crystallization of olivine, orthopyroxene and amphibole over a narrow range of high temperatures between 1055 and 1110°C . In TCG4 and TCG5, temperatures of amphibole crystallization range from ~ 890 to 990°C . These estimates overlap within uncertainty with pyroxene crystallization temperatures of ~ 880 - 910°C estimated from two-pyroxenes thermometer in TCG5 (Table 2; Putirka 2008; uncertainty of $\pm 45^\circ\text{C}$). In TCG6, amphibole crystallization occurs over a large range of

temperature from ~1070°C to ~810°C. The wide range of crystallization temperatures observed for each type of gabbro highlights the importance of melt differentiation during isobaric cooling in the lower arc crust.

In BPT, amphiboles rimming pyroxenes crystallized at ~780-810°C, whereas interstitial amphiboles in BVST record lower temperatures of crystallization ranging from ~665°C to ~730°C (Fig. 9). Tonalites are characterized by distinct pyroxene and amphibole chemistry and systematically lower plagioclase An content (An<55) compared to Tunis Creek gabbros (Figs. 3-6). These results indicate that differentiated tonalitic liquids occur at temperature <800°C in the lower and middle crust at pressure varying from 6-7 to 2-3 kbars. In the BVIS, the range of calculated temperatures and their correlation with mineral chemistry align well with the stochastic thermal and chemical model of Klein and Jagoutz (2021), which showed that a basalt-andesite parental melt must cool near-isobarically to below 850-900°C at pressure >7 kbars to generate the dichotomous crustal structure observed in the BVIS (Fig. 9). Our results further support the elevated thermal regime attributed to high magmatic fluxed and the rapid emplacement in the BVIS (Klein et al. 2021).

7.4 Assessing the parental magma compositions

In the most primitive olivine-bearing Tunis Creek gabbros, olivine, orthopyroxene and clinopyroxene are characterized by relatively evolved Mg#’s and low Al₂O₃ contents. Using mineral-melt partition coefficients $Kd_{olivine}^{Fe-Mg}$, $Kd_{orthopyroxene}^{Fe-Mg}$, and $Kd_{clinopyroxene}^{Fe-Mg}$ of ~0.3 (Supplementary Table S2), these minerals were in equilibrium with melts with Mg#s ranging from 0.4 to 0.6, clearly indicating that these mafic cumulates did not crystallize from primitive arc melt (Mg#>0.65; Kelemen et al. 2014; Schmidt and Jagoutz 2017). Instead, it suggests crystallization from an already differentiated basaltic-andesitic to andesitic parental melt following crystallization of a significant fraction of high Mg# olivine-rich primitive cumulates such as dunite, wherlite, and olivine-websterite (Bucholz et al. 2014a,b; Dessimoz et al. 2012; Jagoutz 2010; Nandedkar et al. 2014; Ulmer et al. 2018). As these cumulates have not been documented in the exposed BVIS, we suggest that they likely formed at greater depths nearer to the Sierran arc Moho. Moreover, these dense ultramafic cumulates could have been recycled to the underlying mantle either through delamination or by mechanical removal of the batholithic root during the shallow slab subduction of the Farallon oceanic lithosphere in the Late Cretaceous (Chapman et al. 2012; Saleeby et al. 2003).

Although the H₂O-contents of BVIS melts are poorly constrained, the co-existence of low Fo olivine and An-rich plagioclase combined with the widespread occurrence of amphibole in Tunis Creek gabbros suggest hydrous parental melts (Arculus and Wills 1980; Panjasawatwong et al. 1995; Sisson and Grove 1993; Tollan et al. 2012; Ushioda et al. 2014). Petrographic observations and amphibole trace element chemistry discussed above show that abundant amphibole crystallized prior to or co-crystallized with plagioclase in TCG2, TCG3 and TCG6, whereas less abundant interstitial amphibole is the last phase in TCG4 and TCG5 (Table 1). Numerous experimental studies have demonstrated that melt H₂O contents strongly control the appearance of amphibole by expanding the amphibole thermal stability field to ~1030-1100 °C at 7-10 kbars (Blatter et al. 2013; Grove et al. 2003; Krawczynski et al. 2012; Melekhova et al.

2013, 2015; Sisson and Grove 1993; Ulmer et al. 2018). Additionally, in hydrous basalts at 7-9 kbars, a minimum of ~3.5 wt. % H₂O in the melt is required to stabilize amphibole at these temperatures (Blatter et al. 2013). Hence, the highest amphibole crystallization temperatures recorded in TCG2, TCG3 and TCG6 (~1050-1070°C; Table 2) require that these gabbros crystallized from melts containing at least 3.5 wt. % H₂O and that amphibole stability in these samples was primarily limited by magma temperatures. In contrast, the highest temperatures recorded by late crystallizing interstitial amphibole found in TCG4 and TCG5 (~980-990°C; Table 2) indicate that the stability of amphibole in these units was dominantly controlled by melt water contents and not temperature. Amphibole in TCG4 and TCG5 only became stable once the differentiation of a less water rich parental magma produced melts with ~3.5 wt. % H₂O.

We can use these observations, combined with the assumption that melt H₂O contents will behave perfectly incompatibly during fractional crystallization prior to amphibole stability, to roughly constrain the initial water contents of BVIS parental melts. Using a range of experimental studies (Blatter et al. 2013; Melekhova et al. 2013, 2015; Nandedkar et al. 2014), we infer that highest temperature amphiboles TCG2, TCG3 and TCG6 crystallized at (primary) melt fractions of 60-80 wt. %, whereas those in TCG4 and TCG5 crystallized after greater extents of fractionation (primary melt fractions of ~20-40 wt. %). This implies that TCG4 and TCG5 crystallized from a damp melt parental with initial H₂O contents of 0.7-1.4 wt. %, while TCG2, TCG3 and TCG5 crystallized from a wet parental melt with minimum initial H₂O contents of 2.1-2.8 wt. %. Based on these constraints, we conclude that the heterogeneous nature of Tunis Creek gabbros is closely related to the presence of parental melts with distinct H₂O contents.

7.5 Genetic link between mafic cumulates and derivative felsic melts

To first order, the complementary major and trace element patterns of BVIS tonalites and Tunis Creek gabbros (Figs. 7 and 8) appear to support a process by which tonalitic liquids were generated by fractionation of these gabbroic cumulates. This process is further supported by the overlapping zircon ages of these two units (Klein et al. 2021). In particular, the onset of fractionation of SiO₂-poor amphibole and An-rich plagioclase in the Tunis Creek gabbros would have played a critical role in generating felsic derivative liquids. In contrast, orthopyroxene has comparable SiO₂ contents to a basaltic-andesite parental melt, and therefore orthopyroxene fractionation is a less efficient mechanism for generating felsic liquids. As amphibole is observed in all Tunis Creek Gabbros, we can test this specific process by comparing the trace element compositions of calculated melts in equilibrium with amphibole to tonalite bulk compositions. Felsic plutonic rocks like the BVIS tonalites can be cumulates formed by removal of erupted melt (Deering and Bachmann, 2010; Gelman et al., 2014; Tavazzani et al., 2020), and it is often difficult to determine the extent to which plutonic rocks with intermediate to felsic compositions represent “true” liquid compositions. However, it has been shown that felsic plutonic rocks (SiO₂ > 55-60 wt. %) often closely resemble liquid composition (e.g., Jagoutz 2014; Kelemen et al. 2014). Owing to the absence of co-genetic/contemporaneous volcanic rocks combined with the lack of petrographic and geochemical evidence for a cumulate origin of tonalites in the BVIS, we assume that the tonalitic compositions represent reasonable estimates of fractionated liquid compositions.

To calculate melt compositions in equilibrium with amphibole, we use amphibole-melt trace element partition coefficients ($Kd_{amph-melt}^{REE}$) derived from fractional crystallization experiments at 7 kbars (Nandedkar et al. 2016), in which amphibole coexists with orthopyroxene, plagioclase and Fe-Ti-oxides at high temperatures (1010–950 °C), and plagioclase and Fe-Ti-oxides at lower temperatures (920–730 °C). These experiments were conducted at pressures and temperatures comparable to the BVIS conditions constrained in the previous sections, and contain comparable mineral assemblages. The closest agreement between trace element compositions in modeled melts in equilibrium with amphiboles in Tunis Creek gabbros and tonalite bulk compositions is found using $Kd_{amph-melt}^{trace\ element}$ from a basaltic-andesite experiment at 1010 °C (RN8inner), while modeled trace element melt concentrations are lower for andesite at 950°C (RN10s) due to higher $Kd_{amph-melt}^{trace\ element}$ (Fig. 10). These results support a co-genetic link between tonalites and Tunis Creek gabbros. and it demonstrates that the multiple parental melts inferred from fractionation sequences documented in the different Tunis Creek Gabbros could all have contributed to the generation of tonalitic derivative melts. Importantly, we re-emphasize that compelling field, petrographic and geochemical evidence argue for fractional crystallization as the primary means of tonalites production in the BVIS. Field evidence for magmatic layering is preserved in gabbros and tonalites (Klein and Jagoutz, 2021), while the absence of migmatite complexes argues against extensive partial melting. Complementary petrography highlights the igneous cumulates textures of Tunis Creek gabbros (Fig. 2c-g) and the mineral chemistry reflects mineral fractionation along with progressive melt differentiation (Figs. 3-5). These features are consistent with the wide range of Tunis Creek mafic cumulates compositions produced by fractional crystallization models, as opposed to partial melting restites that are restricted in compositions (Jagoutz and Klein, 2018).

7.6 Mixing dry and wet parental melts in the deep crust

The Aluminum Saturation Index paradox

Multiple experimental studies have shown that hydrous differentiation at lower crustal pressures generates unusual peraluminous andesitic liquids, with Aluminum Saturation Index (ASI; calculated as molar Al/(Ca + Na + K)) values greater than 1 (Fig. 11; Blatter et al. 2013; Melekhova et al. 2015; Nandedkar et al. 2014; Ulmer et al. 2018). In contrast, typical differentiated arc liquids as observed in the SNB and in the modern Cascades arc characteristically become peraluminous only at significantly more evolved, SiO₂-rich compositions (Fig. 11; Blatter et al. 2013). Based on these observations, the significance of lower crustal fractional crystallization alone for generating felsic crust has been questioned (Blatter et al. 2013, 2017). Instead, it has been proposed that differentiated arc magmas in the SNB and the Cascades are produced either by differentiation of hydrous basalts at middle to upper crustal pressures (1–4 kbars) or by deep crustal mixing between basaltic liquids and highly evolved felsic melts, likely generated by melting of pre-existing crust (Blatter et al. 2013).

Our results, along with previous studies, rule out shallow differentiation in the BVIS as field, petrographic and mineral chemistry all indicate that differentiation dominantly occurred at ≥ 8 kbars (Fig. 9; Chapman et al. 2012; Klein et al. 2021; Nadin and Saleeby 2008; Pickett and Saleeby 1993). However, the

ASI values of BVIS tonalites increase only gradually with increasing SiO₂ contents, and perfectly overlap with compositions from the broader SNB and the Cascades (Fig. 11). Similar evidence for lower crustal fractionation has also been documented in all well-studied arc crustal sections including Kohistan (Jagoutz 2010), Talkeetna (Greene et al. 2006), the North Cascades (Dessimoz et al. 2012), the Gangdese Arc (Guo et al., 2020) and the Famatina Arc (Walker et al. 2015). Additionally, experiments and modeling show that mixing mafic and evolved magmas faces thermally and mechanically difficulties (Laumonier et al. 2014; Sparks and Marshall 1986). These studies show that to fully homogenize, magmas must have nearly equal viscosities after thermally equilibrating. This constraint limits the amount of (lower temperature) evolved melts that can be mixed with basalts to ~<30 vol. %, which in turn limits the composition of hybrid melts produced by mixing to <58 wt. % SiO₂. Mixing with larger evolved melt fractions, causes the basalt to cool and become too viscous and the two end members remains essentially unmixed (Laumonier et al. 2014). This mingling process is frequently documented by the presence of quenched mafic enclaves, schlieren and crystal cargoes in arc magmas (Didier and Barbarin 1991; Jagoutz et al. 2013; Leuthold et al. 2014; Weinberg et al. 2021). Finally, mixing also does not appear consistent with geochemical observations: mixing trends are linear, in contrast to numerous observed differentiation trends which are kinked, as is expected for a shift from incompatible to compatible behavior resulting from changing crystallization assemblage (e.g. TiO₂ and Zr increase until reaching amphibole and zircon stability; Jagoutz 2010).

We believe that the co-existing mafic melts with variable H₂O contents documented in the BVIS suggests an alternative mechanism that is consistent with both the field observations and experimental and modeling constraints. Experimental evidence shows that the initial H₂O content of magmas has a strong effect on the ASI evolution during lower crustal differentiation. Differentiation of dry and water-poor basalts produces minimal ASI enrichment (Melekhova et al. 2015; Villiger et al. 2004, 2007), in contrast to the enrichments produced by hydrous basalts and basaltic andesites (Fig. 11). Thus, we propose that mixing liquids formed by differentiation along wet and dry liquid lines of descent in the lower crust can produce hybrid basalts to andesites with low to moderate water contents and ASI values (Fig. 11). Subsequent differentiation of these magmas can generate the observed trends in the BVIS tonalites. To illustrate the viability of this process, we modeled mixing in the lower crust following the methods described in Sparks and Marshall (1986) and Laumonier et al. (2014), and using experimentally determined wet and dry lower crustal liquid lines of descent (Nandedkar et al. 2014; Villiger et al. 2007). Further details of our mixing calculations are presented in the **Supplementary materials**. Our modeling reproduces the findings of previous workers that hybrid magmas produced by mixing span a restricted range of SiO₂ contents between 48-57 wt. %. Additionally, we find that viable hybrid melts have a larger contribution from the dry melt ($\geq 60\%$) component compared to the hydrous melt ($\leq 40\%$), which restricts hybrid melt compositions to ASI values of ~0.6-0.75 and hybrid melt H₂O contents ranging from 0 to ~3 wt. % (Fig. 11). This range is consistent with our estimates based on amphibole temperatures presented above, and is also significantly lower than melts with comparable SiO₂ contents generated by hydrous differentiation (Nandedkar et al. 2014). Subsequent differentiation of these hybrid melts is expected to be dominated by amphibole +

plagioclase \pm pyroxenes, and thus will produce gradual ASI enrichments. For this range of parental melt compositions, amphibole (\pm Fe-Ti oxides) crystallization is the only effective mechanism to increase both ASI and SiO₂ content of the derivative felsic melt (Fig. 11).

The predominance of orthopyroxene in the BVIS

Lower crustal mixing and limited ASI enrichment also relate to an additional observation from the BVIS – the predominance of orthopyroxene-rich cumulates. Experimental studies show that the stability of orthopyroxene relative to olivine and clinopyroxene primarily depends on melt H₂O content, pressure, and silica activity of the parental melt (Baker et al. 1994; Grove and Kinzler 1986; Kelemen 1995; Krawczynski et al. 2012; Kushiro 1969; Melekhova et al. 2015; Müntener et al. 2001; Sisson and Grove 1993; Ulmer et al. 2018). Typical hydrous fractionation paths are clinopyroxene dominated, which is responsible for the experimentally observed ASI enrichment (Nandedkar et al. 2014; Ulmer et al. 2018). However, the hybrid melts produced by our mixing model have relatively low water contents and increased silica activity, both of which expand the orthopyroxene stability field at the expense of olivine and clinopyroxene (Fig. 12). We speculate that mixing of coexisting wet and dry parental melts has the potential to produce hybrid melts within the stability field of orthopyroxene, which in turn explains the unusual predominance of orthopyroxene and rare clinopyroxene in the BVIS. Fractionation of these orthopyroxene-rich cumulates provides an additional mechanism to limit ASI enrichment. Assimilation of metasedimentary material in the BVIS lower crust, as required by isotopic evidence (Klein et al. 2021; Lackey et al. 2005; Pickett and Saleeby 1994) would likely also increase melt Si activity and expand the orthopyroxene stability field. Enhanced crustal assimilation may have been facilitated by the steep lower crustal geotherm (Fig. 9) caused by high magmatic fluxes during BVIS emplacement (Klein et al. 2021). The destabilization of orthopyroxene at the expense of amphibole crystallization as the melt H₂O contents increase represents the most effective mechanism to explain the formation of co-genetic tonalites (Figs. 7 and 12).

Comparison with other crustal sections

Detailed studies of other arc crustal sections demonstrate that ultramafic-mafic cumulates and derivative felsic intrusions can be produced dominantly by fractional crystallization of a single basaltic parental melt with or without crustal contamination (e.g., Jijal and Chilas complexes in the Kohistan arc, Jagoutz 2010; Jagoutz et al., 2011; Chugach mountains in the Talkeetna arc, Greene et al., 2006; Sierra Valle Fértil – La Huerta in the Famatina arc, Walker et al., 2015; Camilletti et al., 2020; Chelan Complex in the Cascades, Dessimoz et al., 2012; the Dariv Igneous Complex in Western Mongolia, Bucholz et al., 2014b). While these examples demonstrate that mixing of dry and wet mafic magmas is not a prerequisite to produce intermediate to felsic arc crust, we believe that the mixing and differentiation of multiple distinct primary melts is likely a common process in arc lower crust. Geodynamic models show that both decompression and flux melting regimes occur simultaneously in subduction zones (e.g., Conder et al., 2002; Lin et al., 2010), which primarily account for the variations of initial H₂O content in mafic melts as more hydrous melts are produced by flux melting whereas less hydrous melts are formed by decompression melting

(Grove et al. 2002, 2012; Jagoutz et al. 2011). This is documented by (near-)contemporaneous mafic melts with distinct H₂O-contents at numerous arc volcanoes and exposed crustal sections (e.g., Aleutians: Umnak island, Miller et al., 1992; Cascades: Mount Shasta, Grove et al., 2002; Le Voyer et al., 2010; Mount St Helens, Wanke et al., 2019; Gangdese lower crust: Lilong complex, Guo et al. 2020; Izu-Bonin arc: Torishima volcano, Tamura et al., 2007; Sumisu volcano, Tamura et al., 2005; Shirahama Group, Tamura, 1994; Kohistan lower crust: Jijal and Chilas complexes, Jagoutz et al. 2011; Marianas arc: Northwest Rota-1 volcano, Tamura et al., 2011; New Zealand: Taupo volcanic zone, Rooney and Deering, 2014). Moreover, a number of these studies find evidence for mixing between distinct mafic melts with different H₂O contents (e.g., Tamura, 1994; Wanke et al., 2019). Thus we suggest that, at a minimum, the requisite conditions for mixing of wet and dry magmas are common in arc lower crust and that this mixing (possibly combined with assimilation of metasedimentary material) may represent an underappreciated phenomenon and an important step in the formation of felsic arc crust.

We attribute the prevalence of hornblende norite in the BVIS to lower crustal magma mixing and minor crustal assimilation yielding H₂O-poor mafic magmas with elevated silica activities. In contrast, orthopyroxene-rich cumulates are relatively unusual in the majority of exposed arc lower crustal sections (Greene et al., 2006; Jagoutz et al., 2007; Dessimoz et al., 2012; Guo et al., 2020). These lower crustal sections appear to be either dominated by H₂O-rich magmas (e.g., Dessimoz et al., 2010), or have little evidence for crustal assimilation (e.g., Greene et al., 2006), and thus apparently did not generate the melt compositions necessary to stabilize abundant orthopyroxene. Similarly, orthopyroxene-dominated cumulates are not observed in most experimentally constrained arc fractionation sequences (e.g., Blatter et al., 2013; Melekhova et al., 2015; Nandedkar et al., 2014; Ulmer et al., 2018). However, few experiments have evaluated the processes envisaged here, as H₂O-poor differentiation sequences are relatively understudied (Tatsumi and Susuki, 2009; Mandler et al., 2014; Melekhova et al., 2015), and most high pressure (0.7-1 GPa) experimental studies use near-primary mantle melts as starting compositions (Blatter et al., 2013; Melekhova et al., 2015; Nandedkar et al., 2014; Ulmer et al., 2018) that differ significantly from the hypothesized hybrid melts produced by lower crustal mixing in the BVIS.

The one lower crustal section that is lithologically similar to the BVIS is the Sierra Valle Fértil (SVF) in the Famatina arc, which contains mafic cumulates dominated by olivine-bearing hornblende norite (Otamendi et al., 2010, 2012; Walker et al., 2015). In the SVF, evolved Nd and Sr isotopic compositions, as well as abundant metasedimentary migmatites provide strong evidence for the importance of crustal assimilation during differentiation (Otamendi et al., 2008, 2012; Walker et al., 2015). Further, parental melts in the SVF were estimated to have only 1-2 wt. % H₂O (Otamendi et al., 2010). As discussed above, and similar to the BVIS, low H₂O contents and high silica activity in SVF parental melts likely expanded the orthopyroxene stability field at the expense of olivine and clinopyroxene. While lower crustal magma mixing has not been documented in the SVF, neither primary mantle melts nor cumulates in equilibrium with these melts are exposed in this section (Otamendi et al., 2020) and thus generation of these relatively H₂O-poor magmas by mixing hydrous and dry melts at greater depths cannot be fully ruled

out. Finally, we also note that relatively uncommon orthopyroxene-rich hornblende-gabbro norites are present in the lower crust of the Talkeetna Arc, and that it was previously suggested that magma mixing played a role in their petrogenesis (Greene et al., 2006, p. 1078-1079).

Concluding remarks

The Tunis Creek gabbros are characterized by distinct crystallization sequences and mineral chemistry that highlight crystallization from parental melts with different compositions and H₂O contents. The low Mg# and Al₂O₃ compositions of olivine, orthopyroxene and clinopyroxene rules out crystallization from primitive arc magmas and instead suggests crystallization from fractionated basalt-andesite parental magmas. Olivine-bearing gabbros (TCG1, TCG2, TCG3), hornblende and some hornblende gabbro (TCG6) are characterized by the coexistence of low Fo olivine and high An plagioclase and/or the crystallization of high temperature amphibole (1050-1070°C) requiring wet parental melts estimated at least 2.1-2.8 wt. % H₂O. In contrast, the late crystallization of amphibole at lower temperature (<990°C) in hornblende norite (TCG4) and hornblende gabbro norite (TCG5) reflects crystallization from damp parental melts with estimated 0.7-1.4 wt. % H₂O. Collectively, this study demonstrates the presence of co-existing damp and wet parental melts in the lower crust of continental arcs. The hypersthene-bearing tonalites (BPT) and hypersthene-free tonalite (BVST) emplaced in the middle and upper crust crystallized at lower temperatures (700-800°C) and shallower crustal levels. Bulk and mineral geochemistry indicate a co-genetic link between the tonalites and the Tunis Creek gabbros, where tonalitic liquids are produced by the crystallization of amphibole from a basalt-andesite parental melt. The BVST tonalites are characterized by lower ASI values compared to experimental melts produced by differentiation of hydrous primitive melt in the lower crust. Here, we propose a new mixing model whereby dry and hydrous melts mix in the lower crust to produce damp to hydrous hybrid melts with low ASI values. The elegance of this model is that it allows mixing of melts with similar viscosities, yet with variable ASI resulting from differences in initial H₂O content. This model also promotes favorable conditions to expand the orthopyroxene stability field and hence explain the predominance of orthopyroxene crystallization in Tunis Creek gabbros.

Acknowledgements

H. R. acknowledges the support by the Swiss National Foundation early postdoc mobility research grant P2GEP2_178008 and the Swiss National Foundation postdoc mobility grant P400P2_194421. This work was also supported by the National Science Foundation EAR-1552202 to O. J. The authors thank the staff of the Tejon Ranch Conservancy for facilitating our field work. The authors would also like to acknowledge Nilanjan Chatterjee for his technical assistance during EPMA analysis and Craig Martin, Jacob Setera and Jill VanTongeren for their help in LA-ICPMS measurements. We thank George Bergantz and Olivier Bachmann for constructive reviews that helped improving the manuscript, and to the associate editor Mark Ghiorso for handling of the manuscript.

Figure captions

Figure 1 (a) Outline of Sierra Nevada batholith (SNB, California, USA) showing the location of the study area modified after Saleeby et al. (2007), including the contours of igneous emplacement pressures after Ague and Brimhall (1988) and Pickett and Saleeby (1993). (b) Geologic map of the southern SNB showing the Bear Valley Intrusive Suite (BVIS) and surrounding intrusions, metasedimentary wall-rock pendants and volcanic rocks (modified after Nadin and Saleeby 2008; Ross 1989, 1995; Saleeby et al. 2007, 2008). Locations of samples presented in this study are also shown. Range of crystallization ages for the various intrusive suites after Saleeby et al. (2008) and Klein et al. (2021). Thick black lines represent major bounding faults of the southern SNB abbreviated as follows: pKCF – proto-Kern Canyon fault; KCF – Kern Canyon fault; BF – Breckenridge fault GF - Garlock fault; WWF – White Wolf fault.

Figure 2 Photomicrographs of Tunis Creek gabbros (a-g) and tonalites of Bison Peak and Bear Valley Springs (h-i) exposed in the Bear Valley Intrusive Suite. (a) olivine metagabbro with resorbed crystals of olivine and plagioclase combined with altered clinopyroxene. This rock type is characterized by well-developed multi-layers corona texture. (b) Zoom in multi-layers corona texture characterized by orthopyroxene crystallizing at the expense of olivine, which overgrown by amphibole followed by amphibole and green spinel symplectite at the contact with plagioclase. Note the tiny inclusions of pyroxene in plagioclase. (c) olivine-hornblende orthopyroxenite composed of resorbed crystals of olivine within large brown amphibole and adjacent orthopyroxene. (d) olivine-hornblende norite showing olivine, orthopyroxene, plagioclase, large brown amphibole and ilmenite. (e) hornblende norite composed of orthopyroxene and plagioclase with late interstitial brown amphibole. Note the development of cummingtonite between orthopyroxene and amphibole. (f) hornblende gabbro norite showing late interstitial brown amphibole with resorbed orthopyroxene, clinopyroxene and plagioclase. Pyroxene-rich facies characterized by smaller-size clinopyroxene and orthopyroxene crystals is shown on the right-hand side. (g) hornblende gabbro composed of subhedral dark green-beige amphibole and plagioclase together with ilmenite. Note the presence of amphibole inclusions in plagioclase and vice versa. (h) hypersthene-bearing tonalite of Bison Peak characterized by remnants of orthopyroxene overgrown by dark green amphibole and surrounding plagioclase and quartz. (i) tonalite of Bear Valley Springs showing late interstitial light green amphibole and biotite within plagioclase and quartz. Mineral abbreviations: amph – amphibole; bt – biotite; cpx – clinopyroxene; cum – cummingtonite; ilm – ilmenite; ol – olivine; opx – orthopyroxene; plg – plagioclase; qtz – quartz; sp – spinel.

Figure 3 Summary of Mg#s of olivine, orthopyroxene, clinopyroxene, amphibole and anorthite content of plagioclase for the investigated samples in the BVIS.

Figure 4 Al_2O_3 vs. Mg# for orthopyroxene (a) and clinopyroxene (b) crystallized in the BVIS. Composition of orthopyroxene and clinopyroxene crystallized in ultramafic-mafic cumulates of the Chilas complex in Kohistan arc (Jagoutz et al., 2007), Chugach mountains in Talkeetna Arc (DeBari and Coleman 1989; Greene et al. 2006) and Sierra Valle Fértil in Famatina arc (Walker et al. 2015) are also plotted for comparison with other well studied crustal arc sections.

Figure 5 Major element variations of amphibole in the BVIS. (a) Mg# vs. Si. The amphibole names are after the classification scheme of [Leake et al. \(1997\)](#). (b) Al^{IV} vs. $(Na+K)_A$ showing edenite exchange. (c) Al^{IV} vs. Al^{VI} showing Al-Tschermak exchange. (d) Al^{IV} vs. Ca_B showing plagioclase exchange.

Figure 6 Trace element patterns normalized to primitive mantle values ([McDonough and Sun 1995](#)) in (a) orthopyroxene, (b) clinopyroxene, (c) amphibole and (d) plagioclase. The dotted black line represents analytical limit of detection (LOD) for measured elements.

Figure 7 Harker diagrams illustrating the bulk rock composition of Tunis Creek gabbros and tonalite of Bison Peak and Bear Valley Springs. (a) Mg#, (b) K_2O , (c) TiO_2 , (d) Al_2O_3 , (e) Na_2O , (f) FeO_{tot} , (g) CaO , (h) $Eu_N/Eu^* (Eu_N/\sqrt{\sum m_N * Gd_N})$, where N stands for normalized. We also report previously published bulk rock analyses of BVIS intrusions ([Pickett 1991](#); [Ross 1988](#)) and a compilation of bulk rock analyses for the Sierra Nevada batholith downloaded from EarthChem (<https://www.earthchem.org/>).

Figure 8 Trace element patterns normalized to primitive mantle values ([McDonough and Sun 1995](#)) of Tunis Creek gabbros (a, b) and tonalite of Bison Peak and Bear Valley Springs (c). Dotted lines in (a) and (b) represent sample with the occurrence of cummingtonite.

Figure 9 Temperature estimates using the hornblende-plagioclase pair model of [Holland and Blundy \(1994\)](#) at pressure estimated by [Klein and Jagoutz \(2021\)](#) from interpolated pressure surface following the methods of [Nadin and Saleeby \(2008\)](#) and [Chapman et al. \(2012\)](#). Shaded symbols represent temperature estimates using the amphibole only calibration of [Putirka \(2016\)](#). Pressure-Temperature of successful paths of the stochastic thermal and chemical model of [Klein and Jagoutz \(2021\)](#) is shown in the background for comparison, where the grey scale of each path shows the instantaneous melt SiO_2 content (normalized anhydrous) along each modeled path. See section 7.3 for discussion.

Figure 10 Modelled melt compositions normalized in equilibrium with amphibole crystallized in Tunis Creek gabbros compared to bulk rock composition of tonalite of Bison Peak and Bear Valley Springs. (a) The modelled trace element melt compositions are calculated using amphibole trace element partition coefficients of [Nandedkar et al. \(2016\)](#) and normalized to primitive mantle values ([McDonough and Sun 1995](#)).

Figure 11 Variation of Aluminum Saturation Index (molar $Al/(Ca+Na+K)$) vs. SiO_2 (wt.%) for BVIS tonalites (this study, [Pickett 1991](#); [Ross 1988](#)) compared to compiled igneous compositions from the Cascades magmatic arc and Sierra Nevada batholith (pink dots compiled from EarthChem and contour plot after [Blatter et al. \(2013\)](#)), and experimental dry (yellow dots and arrow) and wet (black dots and arrow) liquid lines of descent at 7 kbars from [Villiger et al. \(2007\)](#) and [Nandedkar et al. \(2014\)](#). Squares are plagioclase and amphibole compositions (colors are as in Figure 5), and orthopyroxene and clinopyroxene compositions are indicated with small black arrows. We plot the modeled hybrid melt compositions calculated from our mixing model between dry and wet magmas in the lower crust following the methods described in [Laumonier et al. \(2014\)](#) and further detailed in the [Supplementary materials](#). The color scale indicates the hybrid melt H_2O content from 0 wt. % (blue) to 3 wt. % H_2O (yellow). Red lines show two examples of mixing between dry and wet melts, where the solid red lines show viable hybrid melts, which

are dominantly derived from the dry component. As the wet component increases, the viscosity contrast between the two melts increases and the two end members remain physically unmixed (dashed red line). Stars are labeled with the maximum fraction of wet melt at the transition from mixing to no mixing. See section 7.6 for discussion.

Figure 12 Normative, pseudo-ternary olivine-clinopyroxene-quartz projection from plagioclase after Tormey et al. (1987) showing BVIS tonalites (orange dots) from this study, Pickett (1991) and Ross (1988). The experimental olivine-orthopyroxene-clinopyroxene piercing points are from Grove and Baker (1984) for dry basalt at 8-10 kbars (dry B), from Ulmer et al. (2018) for wet basaltic andesite at 10 kbars and 5 wt. % H₂O (wet BA), and from Nandedkar et al. (2014) for wet basalt at 7 kbars and 3 wt. % H₂O (wet B). We plot the modeled hybrid melt compositions calculated using our mixing model as in Figure 11. The liquid line of descent of basaltic andesite and approximate phase boundaries (grey lines) from Ulmer et al. (2018) is shown for reference. See section 7.6 for discussion. Range of mineral compositions crystallized in Tunis Creek gabbros are shown with colored fields, where squares represent amphiboles crystallized in the different types of Tunis Creek gabbros (colors are as in Figure 5). Mineral abbreviations: amph – amphibole; cpx – clinopyroxene; ol – olivine; opx – orthopyroxene; qtz – quartz.

References

- Ague JJ (1997) Thermodynamic calculation of emplacement pressures for batholithic rocks, California: Implications for the aluminum-in-hornblende barometer. *Geology* 25:563–566. [https://doi.org/10.1130/0091-7613\(1997\)025<0563:TCOEPF>2.3.CO;2](https://doi.org/10.1130/0091-7613(1997)025<0563:TCOEPF>2.3.CO;2)
- Ague JJ, Brimhall GH (1988) Magmatic arc asymmetry and distribution of anomalous plutonic belts in the batholiths of California: Effects of assimilation, crustal thickness, and depth of crystallization. *Bull Geol Soc Am* 100:912–927. [https://doi.org/10.1130/0016-7606\(1988\)100<0912:MAAADO>2.3.CO;2](https://doi.org/10.1130/0016-7606(1988)100<0912:MAAADO>2.3.CO;2)
- Annen C, Blundy JD, Sparks RSJ, Gene DE (2006) The Genesis of Intermediate and Silicic Magmas in Deep Crustal Hot Zones. *J Petrol* 47:505–539. <https://doi.org/10.1093/petrology/egi084>
- Arculus RJ, Wills KJA (1980) The petrology of plutonic blocks and inclusions from the lesser antilles Island arc. *J Petrol* 21:743–799. <https://doi.org/10.1093/petrology/21.4.743>
- Armstrong JT (1995) CITZAF - A package of correction programs for the quantitative electron microbeam X-ray analysis of thick polished materials, thin-films, and particles. *Microbeam Anal* 4:177–200.
- Arndt NT, Goldstein SL (1989) An open boundary between lower continental crust and mantle: its role in crust formation and crustal recycling. *Tectonophysics* 161:201–212. [https://doi.org/10.1016/0040-1951\(89\)90154-6](https://doi.org/10.1016/0040-1951(89)90154-6)
- Ashworth JR (1986) The role of magmatic reaction, diffusion, and annealing in the evolution of coronitic microstructure in troctolitic gabbro from Risør, Norway: a discussion. *Mineral Mag* 50:469–473. <https://doi.org/10.1180/minmag.1986.050.357.09>
- Baker MB, Grove TL, Price R (1994) Primitive basalts and andesites from the Mt. Shasta region, N. California: products of varying melt fraction and water content. *Contrib to Mineral Petrol* 118:111–129. <https://doi.org/10.1007/BF01052863>
- Beattie P (1993) Olivine-melt and orthopyroxene-melt equilibria. *Contrib to Mineral Petrol* 115:103–111. <https://doi.org/10.1007/BF00712982>
- Blatter DL, Sisson TW, Hankins WB (2017) Voluminous arc dacites as amphibole reaction-boundary liquids. *Contrib to Mineral Petrol* 172:27. <https://doi.org/10.1007/s00410-017-1340-6>
- Blatter DL, Sisson TW, Hankins WB (2013) Crystallization of oxidized, moderately hydrous arc basalt at mid- to lower-crustal pressures: implications for andesite genesis. *Contrib to Mineral Petrol* 166:861–886. <https://doi.org/10.1007/s00410-013-0920-3>
- Bucholz CE, Jagoutz O, Schmidt MW, Sambuu O (2014a) Phlogopite- and clinopyroxene-dominated fractional crystallization of an alkaline primitive melt: petrology and mineral chemistry of the Dariv Igneous Complex, Western Mongolia. *Contrib to Mineral Petrol* 167:994. <https://doi.org/10.1007/s00410-014-0994-6>
- Bucholz CE, Jagoutz O, Schmidt MW, Sambuu O (2014b) Fractional crystallization of high-K arc magmas: biotite- versus amphibole-dominated fractionation series in the Dariv Igneous Complex, Western Mongolia. *Contrib to Mineral Petrol* 168:1072. <https://doi.org/10.1007/s00410-014-1072-9>

- Camilletti G, Otamendi J, Tibaldi A, Cristofolini E, Leisen M, Romero R, Barra F, Armas P, Barzola M. (2020). Geology, petrology and geochronology of sierra Valle Fértil-La Huerta batholith: implications for the construction of a middle-crust magmatic-arc section. *Journal of South American Earth Sciences*, 97, 102423. <https://doi.org/10.1016/j.jsames.2019.102423>
- Chapman A (2012) Late Cretaceous gravitational collapse of the southern Sierra Nevada batholith, California. *Geosphere* 8:314-341. <https://doi.org/10.1130/GES00740.1>
- Chen JH, Moore JG (1982) Uranium-lead isotopic ages from the Sierra Nevada batholith, California. *J Geophys Res* 87:4761-4784. <https://doi.org/10.1029/JB087iB06p04761>
- Clemens JD, Stevens G (2012) What controls chemical variation in granitic magmas? *Lithos* 134-135:317-329. <https://doi.org/10.1016/j.lithos.2012.01.001>
- Clemens JD, Stevens G, Farina F (2011) The enigmatic sources of I-type granites: The peritectic connexion. *Lithos* 126:174–181. <https://doi.org/10.1016/j.lithos.2011.07.004>
- Coleman DS, Glazner AF (1997) The sierra crest magmatic event: Rapid formation of juvenile crust during the late cretaceous in California. *Int Geol Rev* 39:768–787. <https://doi.org/10.1080/00206819709465302>
- Conder JA, Wiens DA, Morris J (2002) On the decompression melting structure at volcanic arcs and back-arc spreading centers, *Geophys. Res. Lett.*, 29:1727. [10.1029/2002GL015390](https://doi.org/10.1029/2002GL015390)
- Das T, Nolet G (1998) Crustal thickness map of the western United States by partitioned waveform inversion. *J Geophys Res Solid Earth* 103:30021–30038. <https://doi.org/10.1029/98jb01119>
- Davidson JP, Arculus RJ (2005) The significance of Phanerozoic arc magmatism in generating continental crust, in Brown, M., and Rushmer, T., editors, *Evolution and Differentiation of the Continental Crust*: Cambridge, England, Cambridge University Press, p. 135–172.
- de Haas GJLM, Nijland TG, Valbracht PJ, Maijer C, Verschure R, Andersen T (2002) Magmatic versus metamorphic origin of olivine-plagioclase coronas. *Contrib to Mineral Petrol* 143:537-550. <https://doi.org/10.1007/s00410-002-0362-9>
- Debari SM, Coleman RG (1989) Examination of the deep levels of an island arc: evidence from the Tonsina ultramafic-mafic assemblage, Tonsina, Alaska. *J Geophys Res* 94:4373–4391. <https://doi.org/10.1029/JB094iB04p04373>
- Deering CD, Bachmann O (2010) Trace element indicators of crystal accumulation in silicic igneous rocks. *Earth Planet Sci Lett* 297(1-2):324-331 doi:10.1016/J.Epsl.2010.06.034
- DePaolo DJ (1981) Trace element and isotopic effects of combined wallrock assimilation and fractional crystallization. *Earth Planet Sci Lett* 53:189–202. [https://doi.org/10.1016/0012-821X\(81\)90153-9](https://doi.org/10.1016/0012-821X(81)90153-9)
- Dessimoz M, Müntener O, Ulmer P (2012) A case for hornblende dominated fractionation of arc magmas: the Chelan Complex (Washington Cascades). *Contrib to Mineral Petrol* 163:567–589. <https://doi.org/10.1007/s00410-011-0685-5>
- Didier J, Barbarin B (1991) The different types of enclaves in granites - Nomenclature. *Developments in Petrology* 13. Enclaves and Granite Petrology. 19-23.

- Dixon ET (1995) An Evaluation of Hornblende Barometry, Isabella to Tehachapi Region, Southern Sierra Nevada, California [M.S. thesis]: Ann Arbor, University of Michigan, 150 p.
- Dodge FCW, Calk LC, Kistler RW (1986) Lower Crustal Xenoliths, Chinese Peak Lava Flow, Central Sierra Nevada. *J Petrol* 27:1277–1304. <https://doi.org/10.1093/petrology/27.6.1277>
- Ducea M (2001) The California arc: Thick granitic batholiths, eclogitic residues, lithospheric-scale thrusting, and magmatic flare-ups. *GSA Today*. [https://doi.org/10.1130/1052-5173\(2001\)011<0004:TCATGB>2.0.CO;2](https://doi.org/10.1130/1052-5173(2001)011<0004:TCATGB>2.0.CO;2)
- Ducea MN, Barton MD (2007) Igniting flare-up events in Cordilleran arcs. *Geology* 35:1047–1050. <https://doi.org/10.1130/G23898A.1>
- Ducea MN, Saleeby JB (1998) The age and origin of a thick mafic-ultramafic keel from beneath the Sierra Nevada batholith. *Contrib to Mineral Petrol* 133:169–185. <https://doi.org/10.1007/s004100050445>
- Ducea MN, Bergantz GW, Crowley JL, Otamendi J (2017). Ultrafast magmatic buildup and diversification to produce continental crust during subduction. *Geology*, 45(3), 235–238. doi:10.1130/G38726.1
- Flidner MM, Klemperer SL, Christensen NI (2000) Three-dimensional seismic model of the Sierra Nevada arc, California, and its implications for crustal and upper mantle composition. *J Geophys Res Solid Earth* 105:10899–10921. <https://doi.org/10.1029/2000jb900029>
- Gallien F, Mogessie A, Hauzenberger CA, Bjerg E, Delpino S, Castro de Machuca B (2012) On the origin of multi-layer coronas between olivine and plagioclase at the gabbro-granulite transition, Valle Fértil-La Huerta Ranges, San Juan Province, Argentina. *J Metamorph Geol* 30:281–302. <https://doi.org/10.1111/j.1525-1314.2011.00967.x>
- Gelman S, Deering C, Bachmann O, Huber C, Gutiérrez F (2014). Identifying the crystal graveyards remaining after large silicic eruptions. *Earth Planet Sci Lett* 403:299–306. <http://doi.org/10.1016/j.epsl.2014.07.005>
- Glazner AF (1991) Plutonism, oblique subduction, and continental growth: an example from the Mesozoic of California. *Geology* 19:784–786. [https://doi.org/10.1130/0091-7613\(1991\)019<0784:POSACG>2.3.CO;2](https://doi.org/10.1130/0091-7613(1991)019<0784:POSACG>2.3.CO;2)
- Greene AR, DeBari SM, Kelemen PB, Blusztajm J, Clift PD (2006) A Detailed Geochemical Study of Island Arc Crust: the Talkeetna Arc Section, South–Central Alaska. *J Petrol* 47:1051–1093. <https://doi.org/10.1093/petrology/egl002>
- Grove TL, Baker B (1984) Phase equilibrium controls on the tholeiitic versus calc-alkaline differentiation trends. *J Geophys Res Solid Earth* 89:3253–3274. <https://doi.org/10.1029/JB089iB05p03253>
- Grove TL, Kinzler RJ (1986) Petrogenesis of Andesites. *Annu Rev Earth Planet Sci* 14:417–454. <https://doi.org/10.1146/annurev.ea.14.050186.002221>
- Grove TL, Parman S, Bowring S, Price R, Baker M (2002) The role of an H₂O-rich fluid component in the generation of primitive basaltic andesites and andesites from the Mt. Shasta region, N California. *Contrib to Mineral Petrol* 142:375–396. <https://doi.org/10.1007/s004100100299>
- Grove TL, Elkins-Tanton LT, Parman SW, Chatterjee N, Müntener O, Gaetani GA (2003) Fractional

- 897 crystallization and mantle-melting controls on calc-alkaline differentiation trends. *Contrib to Mineral*
 898 *Petrol* 145:515–533. <https://doi.org/10.1007/s00410-003-0448-z>
- 899 Grove TL, Till CB, Krawczynski MJ (2012) The Role of H₂O in Subduction Zone Magmatism. *Annu Rev*
 900 *Earth Planet Sci* 40:413–439. <https://doi.org/10.1146/annurev-earth-042711-105310>
- 901 Guo L, Jagoutz O, Shinevar WJ, Zhang HF (2020) Formation and composition of the Late Cretaceous
 902 Gangdese arc lower crust in southern Tibet. *Contrib to Mineral Petrol* 175:1–26.
 903 <https://doi.org/10.1007/s00410-020-01696-y>
- 904 Hacker BR, Mehl L, Kelemen PB, Rioux M, Behn MD, Luffi P (2008) Reconstruction of the Talkeetna
 905 intraoceanic arc of Alaska through thermobarometry. *J Geophys Res Solid Earth* 113:B03.
 906 <https://doi.org/10.1029/2007JB005208>
- 907 Helmy HM, Yoshikawa M, Shibata T, Arai S, Tamura A (2008) Corona structure from arc mafic-
 908 ultramafic cumulates: The role and chemical characteristics of late-magmatic hydrous liquids. *J Mineral*
 909 *Petrol Sci* 103:333–344. <https://doi.org/10.2465/jmps.070906>
- 910 Herzberg C, O'Hara MJ (2002) Plume-associated ultramafic magmas of phanerozoic age. *J Petrol* 43:
 911 1857–1883. <https://doi.org/10.1093/petrology/43.10.1857>
- 912 Hildreth W, Moorbath S (1988) Crustal contributions to arc magmatism in the Andes of Central Chile.
 913 *Contrib to Mineral Petrol* 98:455–489. <https://doi.org/10.1007/BF00372365>
- 914 Holland T, Blundy J (1994) Non-ideal interactions in calcic amphiboles and their bearing on amphibole-
 915 plagioclase thermometry. *Contrib to Mineral Petrol* 116:433–447. <https://doi.org/10.1007/BF00310910>
- 916 Jagoutz O (2014) Arc crustal differentiation mechanisms. *Earth Planet Sci Lett* 396:267–277.
 917 <https://doi.org/10.1016/j.epsl.2014.03.060>
- 918 Jagoutz O, Behn MD (2013) Foundering of lower island-arc crust as an explanation for the origin of the
 919 continental Moho. *Nature* 504:131–134. <https://doi.org/10.1038/nature12758>
- 920 Jagoutz O, Kelemen PB (2015) Role of Arc Processes in the Formation of Continental Crust. *Annu Rev*
 921 *Earth Planet Sci* 43:363–404. <https://doi.org/10.1146/annurev-earth-040809-152345>
- 922 Jagoutz O, Klein B (2018) On the importance of crystallization-differentiation for the generation of SiO₂-
 923 rich melts and the compositional build-up of arc (and continental) crust. *Am J Sci* 318:29–63.
 924 <https://doi.org/10.2475/01.2018.03>
- 925 Jagoutz O, Müntener O, Schmidt MW, Burg J-P (2011) The roles of flux- and decompression melting and
 926 their respective fractionation lines for continental crust formation: Evidence from the Kohistan arc.
 927 *Earth Planet Sci Lett* 303:25–36. <https://doi.org/10.1016/J.EPSL.2010.12.017>
- 928 Jagoutz O, Müntener O, Ulmer P, Pettke T, Burg JP, Dawood H, Hussain S (2007) Petrology and mineral
 929 chemistry of lower crustal intrusions: The chilas complex, Kohistan (NW Pakistan). *J Petrol* 48:1895–
 930 1953. <https://doi.org/10.1093/petrology/egm044>
- 931 Jagoutz O, Schmidt MW (2012) The formation and bulk composition of modern juvenile continental crust:
 932 The Kohistan arc. *Chem Geol* 298–299:79–96. <https://doi.org/10.1016/j.chemgeo.2011.10.022>
- 933 Jagoutz O, Schmidt MW, Enggist A, Burg JP, Hamid D, Hussain S (2013) TTG-type plutonic rocks formed

- in a modern arc batholith by hydrous fractionation in the lower arc crust. *Contrib to Mineral Petrol* 166:1099–1118. <https://doi.org/10.1007/s00410-013-0911-4>
- Jagoutz OE (2010) Construction of the granitoid crust of an island arc. Part II: A quantitative petrogenetic model. *Contrib to Mineral Petrol* 160:359–381. <https://doi.org/10.1007/s00410-009-0482-6>
- Jagoutz OE, Burg JP, Hussain S, Dawood H, Pettke T, Lizuka T, Maruyama S (2009) Construction of the granitoid crust of an island arc part I: Geochronological and geochemical constraints from the plutonic Kohistan (NW Pakistan). *Contrib to Mineral Petrol* 158:739–755. <https://doi.org/10.1007/s00410-009-0408-3>
- Joesten R (1986) The role of magmatic reaction, diffusion and annealing in the evolution of coronitic microstructure in troctolitic gabbro from Risør, Norway. *Mineral Mag* 50:441–467. <https://doi.org/10.1180/minmag.1986.050.357.08>
- Jull M, Kelemen PB (2001) On the conditions for lower crustal convective instability. *J Geophys Res Solid Earth* 106:6423–6446. <https://doi.org/10.1029/2000jb900357>
- Kay RW, Mahlburg Kay S (1993) Delamination and delamination magmatism. *Tectonophysics* 219:177–189. [https://doi.org/10.1016/0040-1951\(93\)90295-U](https://doi.org/10.1016/0040-1951(93)90295-U)
- Kelemen PB (1995) Genesis of high Mg# andesites and the continental crust. *Contrib to Mineral Petrol* 120:1–19. <https://doi.org/10.1007/BF00311004>
- Kelemen PB, Hanghøj K, Greene AR (2014) One view of the geochemistry of subduction-related magmatic arcs, with an emphasis on primitive andesite and lower crust. *Treatise on geochemistry* 4:749–806. <http://dx.doi.org/10.1016/B978-0-08-095975-7.00323-5>
- Klein BZ, Jagoutz O (2021) Construction of a trans-crustal magma system: Building the Bear Valley Intrusive Suite, southern Sierra Nevada, California. *Earth Planet Sci Lett* 553:116624. <https://doi.org/10.1016/j.epsl.2020.116624>
- Klein BZ, Jagoutz O, Ramezani J (2020) High-precision geochronology requires that ultrafast mantle-derived magmatic fluxes built the transcrustal Bear Valley Intrusive Suite, Sierra Nevada, California, USA. *Geology* 49:106–110. <https://doi.org/10.1130/G47952.1>
- Krawczynski MJ, Grove TL, Behrens H (2012) Amphibole stability in primitive arc magmas: effects of temperature, H₂O content, and oxygen fugacity. *Contrib to Mineral Petrol* 164:317–339. <https://doi.org/10.1007/s00410-012-0740-x>
- Kushiro I (1969) The system forsterite-diopside-silica with and without water at high pressures. *Am. J. Sci.* 267:269–294
- Kushiro I, Yoder HS (1966) Anorthite-Forsterite and Anorthite-Enstatite Reactions and their bearing on the Basalt–Eclogite Transformation. *J Petrol* 7:337–362. <https://doi.org/10.1093/petrology/7.3.337>
- Lackey JS, Valley JW, Saleeby JB (2005) Supracrustal input to magmas in the deep crust of Sierra Nevada batholith: Evidence from high- $\delta^{18}\text{O}$ zircon. *Earth Planet Sci Lett* 235:315–330. <https://doi.org/10.1016/j.epsl.2005.04.003>
- Laumonier M, Scaillet B, Pichavant M, Champallier R, Andujar J, Arbaret L (2014) On the conditions of

- 971 magma mixing and its bearing on andesite production in the crust. *Nat Commun* 5:1-12.
- 972 <https://doi.org/10.1038/ncomms6607>
- 973 Leake BE, Woolley AR, Arps CES, Birch WD, Gilbert MC, Grice JD, Hawthorne FC, Kato A, Kisch HJ,
- 974 Krivovichev VG, Linthout K, Laird J, Mandarino J, Maresch WV, Nickel EH, Rock NMS, Schumacher
- 975 JC, Smith DC, Stephenson NCN, Yngaretti L, Whittaker EJW, Youzhi G (1997) Nomenclature of
- 976 amphiboles: Report of the subcommittee on amphiboles of the international mineralogical association,
- 977 commission on new minerals and mineral names. *Min Mag* 61:295-310.
- 978 <https://doi.org/10.1180/minmag.1997.061.405.13>
- 979 Lee CTA, Cheng X, Horodyskyj U (2006) The development and refinement of continental arcs by primary
- 980 basaltic magmatism, garnet pyroxenite accumulation, basaltic recharge and delamination: Insights from
- 981 the Sierra Nevada, California. *Contrib to Mineral Petrol* 151:222–242. [https://doi.org/10.1007/s00410-](https://doi.org/10.1007/s00410-005-0056-1)
- 982 [005-0056-1](https://doi.org/10.1007/s00410-005-0056-1)
- 983 Leuthold J, Müntener O, Baumgartner LP, Putlitz B (2014) Petrological constraints on the recycling of
- 984 mafic crystal mushes and intrusion of braided sills in the Torres del Paine mafic complex (Patagonia). *J*
- 985 *Petrol* 55:917-949. <https://doi.org/10.1093/petrology/egu011>
- 986 Le Voyer M, Rose-Koga EF, Shimizu N, Grove TL, Schiano P (2010) Two contrasting H₂O-rich
- 987 components in primary melt inclusions from Mount Shasta. *J Petrol* 51:1571–1595,
- 988 [doi:10.1093/petrology/egq030](https://doi.org/10.1093/petrology/egq030).
- 989 Li L, Xiong XL, Liu XC (2017) Nb/Ta Fractionation by Amphibole in Hydrous Basaltic Systems:
- 990 Implications for Arc Magma Evolution and Continental Crust Formation. *J Petrol* 58:3-28.
- 991 <https://doi.org/10.1093/petrology/egw070>
- 992 Lin S-C, B-Y Kuo, S-L Chung (2010) Thermomechanical models for the dynamics and melting processes
- 993 in the Mariana subduction system. *J Geophys Res* 115:B12403. [doi:10.1029/2010JB007658](https://doi.org/10.1029/2010JB007658)
- 994 Malin PE, Goodman ED, Henyey TL, Li YG, Okaya DA, Saleeby JB (1995) Significance of seismic
- 995 reflections beneath a tilted exposure of deep continental crust, Tehachapi Mountains, California. *J*
- 996 *Geophys Res Solid Earth* 100:2069–2087. <https://doi.org/10.1029/94JB02127>
- 997 Mandler BE, Donnelly-Nolan JM, Grove TL (2014) Straddling the tholeiitic/calc-alkaline transition: the
- 998 effects of modest amounts of water on magmatic differentiation at Newberry Volcano, Oregon.
- 999 *Contrib to Mineral Petrol* 168:1066. <https://doi.org/10.1007/s00410-014-1066-7>
- 1000 McDonough WF, Sun S-s. (1995) The composition of the earth. *Chem Geol* 120:223-253. [https://doi.org/10.1016/0009-2541\(94\)00140-4](https://doi.org/10.1016/0009-2541(94)00140-4)
- 1001
- 1002 Médard E, Grove TL (2008) The effect of H₂O on the olivine liquidus of basaltic melts: Experiments and
- 1003 thermodynamic models. *Contrib to Mineral Petrol* 155:417-432. [https://doi.org/10.1007/s00410-007-](https://doi.org/10.1007/s00410-007-0250-4)
- 1004 [0250-4](https://doi.org/10.1007/s00410-007-0250-4)
- 1005 Melekhova E, Annen C, Blundy J (2013) Compositional gaps in igneous rock suites controlled by magma
- 1006 system heat and water content. *Nat Geosci* 6:385–390. <https://doi.org/10.1038/ngeo1781>
- 1007 Melekhova E, Blundy J, Robertson R, Humphreys MCS (2015) Experimental Evidence for Polybaric

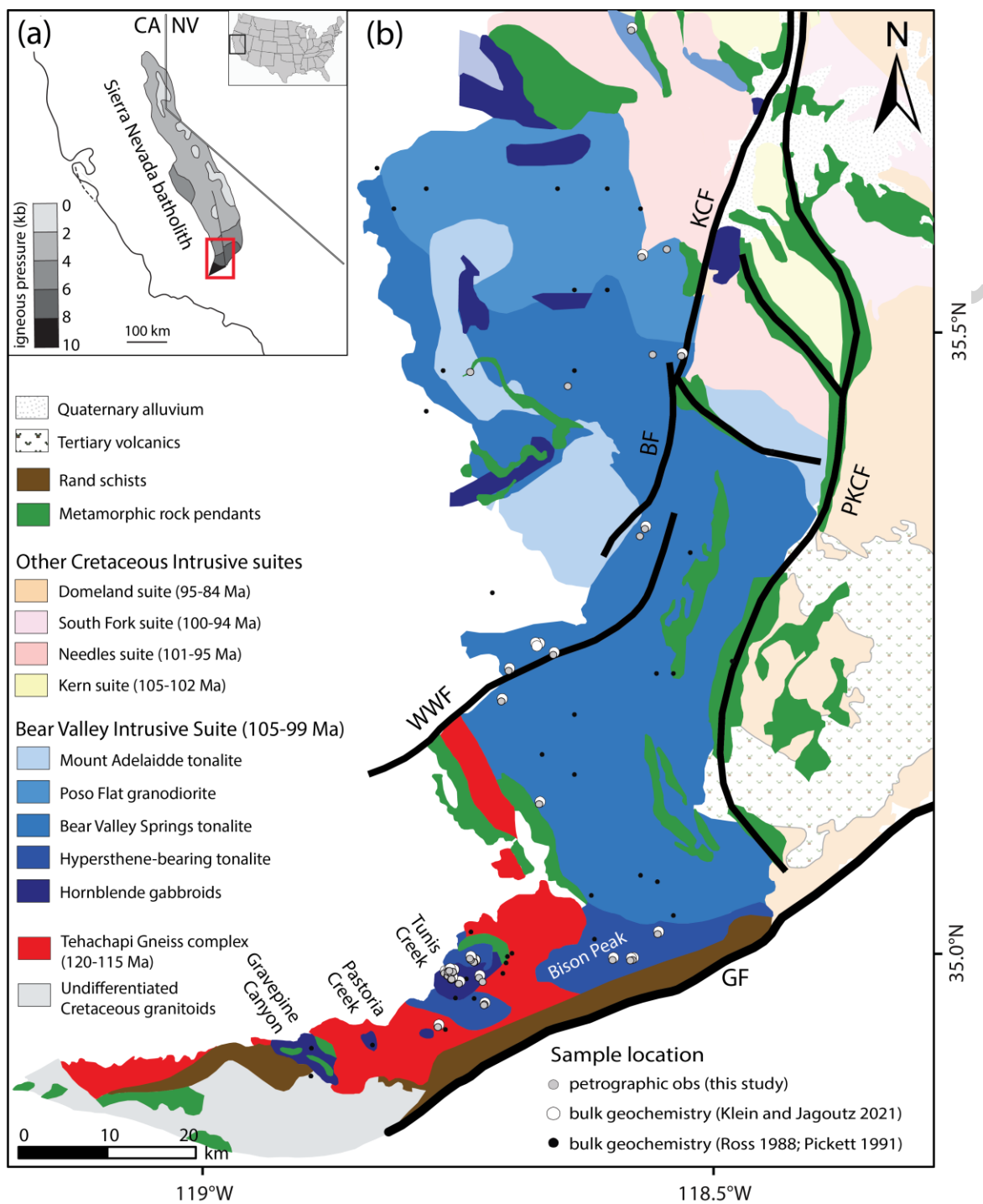
- 1008 Differentiation of Primitive Arc Basalt beneath St. Vincent, Lesser Antilles. *J Petrol* 56:161–192.
- 1009 <https://doi.org/10.1093/petrology/egu074>
- 1010 Miller DM, Langmuir CH, Goldstein SL, Franks AL (1992) The importance of parental magma
- 1011 composition to calc-alkaline and tholeiitic evolution: Evidence from Umnak Island in the Aleutians. *J*
- 1012 *Geophys Res* 97:321–343. <https://doi.org/10.1029/91JB02150>
- 1013 Mooney WD, Weaver CS (1989) Chapter 9: Regional crustal structure and tectonics of the Pacific Coastal
- 1014 States; California, Oregon, and Washington. *Mem Geol Soc Am*. <https://doi.org/10.1130/MEM172->
- 1015 [p129](https://doi.org/10.1130/MEM172-p129)
- 1016 Müntener O, Ulmer P (2018) Arc crust formation and differentiation constrained by experimental
- 1017 petrology. *Am J Sci* 318:64–89. <https://doi.org/10.2475/01.2018.04>
- 1018 Nadin ES, Saleeby J, Wong M (2016) Thermal evolution of the Sierra Nevada batholith, California, and
- 1019 implications for strain localization. *Geosphere* 12:377–399. <https://doi.org/10.1130/GES01224.1>
- 1020 Nadin ES, Saleeby JB (2008) Disruption of regional primary structure of the Sierra Nevada batholith by the
- 1021 Kern Canyon fault system, California. *Spec Pap* 438 Ophiolites, Arcs, Batholiths A Tribut to Cliff
- 1022 Hopson 2438:429–454. [https://doi.org/10.1130/2008.2438\(15\)](https://doi.org/10.1130/2008.2438(15))
- 1023 Nandedkar RH, Hürlimann N, Ulmer P, Müntener O (2016) Amphibole–melt trace element partitioning of
- 1024 fractionating calc-alkaline magmas in the lower crust: an experimental study. *Contrib to Mineral Petrol*
- 1025 171:71. <https://doi.org/10.1007/s00410-016-1278-0>
- 1026 Nandedkar RH, Ulmer P, Müntener O (2014) Fractional crystal- lization of primitive, hydrous arc magmas:
- 1027 an experimental study at 0.7 GPa. *Contrib Miner Petrol* 167:1015. [https://doi.org/10.1007/s00410-](https://doi.org/10.1007/s00410-014-1015-5)
- 1028 [014-1015-5](https://doi.org/10.1007/s00410-014-1015-5)
- 1029 Niu Y, Gilmore T, Mackie S, Greig A, Bach W (2002) Mineral chemistry, whole-rock compositions, and
- 1030 petrogen- esis of Leg 176 gabbros: data and discussion. In: Natland, J.H., Dick, H.J.B., Miller, D.J. &
- 1031 Von Herzen, R.P. (eds) *Proc. ODP, Sci. Results*, 176, 1–60.
- 1032 Otamendi JE, Tibaldi AM, Vujovich GI, Viñao GA (2008) Metamorphic evolution of migmatites from the
- 1033 deep Famatinian arc crust exposed in Sierras Valle Fértil–La Huerta, San Juan, Argentina. *J South Am*
- 1034 *Earth Sci* 25(3):313–335. <https://doi.org/10.1016/j.jsames.2007.09.001>
- 1035 Otamendi JE, Cristofolini E, Tibaldi AM, Quevedo FI, Baliani I (2010) Petrology of mafic and ultramafic
- 1036 layered rocks from the Jabon- cillo Valley, Sierra de Valle Fértil, Argentina: implications for the
- 1037 evolution of magmas in the lower crust of the Famatinian arc. *J South Am Earth Sci* 29:685–704. [https](https://doi.org/10.1016/j.jsame s.2009.11.001)
- 1038 [://doi.org/10.1016/j. jsame s.2009.11.001](https://doi.org/10.1016/j.jsame s.2009.11.001)
- 1039 Otamendi JE, Ducea MN, Bergantz GW (2012) Geological, Petrological and Geochemical Evidence for
- 1040 Progressive Construction of an Arc Crustal Section, Sierra de Valle Fertil, Famatinian Arc, Argentina. *J*
- 1041 *Petrol* 53:761–800. <https://doi.org/10.1093/petrology/egr079>
- 1042 Otamendi JE, Cristofolini EA, Morosini A, Armas P, Tibaldi AM, Camilletti GC (2020). The geodynamic
- 1043 history of the Famatinian arc, Argentina: a record of exposed geology over the type section (latitudes

- 1044 27°-33° south). *Journal of South American Earth Sciences*, 100, 102558.
- 1045 <https://doi.org/10.1016/j.jsames.2020.102558>
- 1046 Panjasawatwong Y, Danyushevsky L V., Crawford AJ, Harris KL (1995) An experimental study of the
- 1047 effects of melt composition on plagioclase-melt equilibria at 5 and 10 kbar: implications for the origin
- 1048 of magmatic high-An plagioclase. *Contrib to Mineral Petrol* 118:420–432.
- 1049 <https://doi.org/10.1007/s004100050024>
- 1050 Paterson SR, Ducea MN (2015) Arc magmatic tempos: Gathering the evidence. *Elements* 11:91-98.
- 1051 <https://doi.org/10.2113/gselements.11.2.91>
- 1052 Patiño Douce AE (1995) Experimental generation of hybrid silici melts by reaction of high-Al basalt with
- 1053 metamorphic rocks. *J Geophys Res* 100, 15623-15639. <https://doi.org/10.1029/94JB03376>
- 1054 Pickett, D.A. (1991) An isotopic and petrologic study of an exposure of the deep Sierra Nevada batholith,
- 1055 Tehachapi Mountains, California. *Unpublished PhD Thesis*. California Institute of Technology.
- 1056 Pickett D, Saleeby JB (1994) Nd, Sr, and Pb isotopic characteristics of Cretaceous intrusive rocks from
- 1057 deep levels of the Sierra Nevada batholith, Tehachapi Mountains, California. *Contrib to Mineral Petrol*
- 1058 118:198–215. <https://doi.org/10.1007/BF01052869>
- 1059 Pickett DA, Saleeby JB (1993) Thermobarometric constraints on the depth of exposure and conditions of
- 1060 plutonism and metamorphism at deep levels of the Sierra Nevada Batholith, Tehachapi Mountains,
- 1061 California. *J Geophys Res* 98:609–629. <https://doi.org/10.1029/92JB01889>
- 1062 Putirka K (2016) Amphibole thermometers and barometers for igneous systems and some implications for
- 1063 eruption mechanisms of felsic magmas at arc volcanoes. *Am Mineral* 101:841-858.
- 1064 <https://doi.org/10.2138/am-2016-5506>
- 1065 Putirka KD (2008) Thermometers and Barometers for Volcanic Systems. *Rev Mineral Geochemistry*
- 1066 69:61–120. <https://doi.org/10.2138/rmg.2008.69.3>
- 1067 Rapp RP, Watson EB (1995) Dehydration melting of metabasalt at 8-32 kbar: Implications for continental
- 1068 growth and crust-mantle recycling. *J Petrol* 36:891-931. <https://doi.org/10.1093/petrology/36.4.891>
- 1069 Ratajeski K, Sisson TW, Glazner AF (2005) Experimental and geochemical evidence for derivation of the
- 1070 El Capitan Granite, California, by partial melting of hydrous gabbroic lower crust. *Contrib to Mineral*
- 1071 *Petrol* 149:713-734. <https://doi.org/10.1007/s00410-005-0677-4>
- 1072 Roberts MP, Clemens JD (1993) Origin of high-potassium, calc-alkaline, I-type granitoids. *Geology*
- 1073 21:825-828. [https://doi.org/10.1130/0091-7613\(1993\)021<0825:OOHPTA>2.3.CO](https://doi.org/10.1130/0091-7613(1993)021<0825:OOHPTA>2.3.CO)
- 1074 Roeder PL, Emslie RF (1970) Olivine-liquid equilibrium. *Contrib to Mineral Petrol* 29:275-289.
- 1075 <https://doi.org/10.1007/BF00371276>
- 1076 Rooney TO, Deering CD (2014) Conditions of melt generation beneath the Taupo Volcanic Zone: The
- 1077 influence of heterogeneous mantle inputs on large-volume silicic systems. *Geology* 42(1), 3–6.
- 1078 10.1130/G34868.1.

- 1079 Ross DC (1995) Reconnaissance Geologic Map of the Southern Sierra Nevada, Kern, Tulare, and Inyo
1080 Counties, California. *U.S. Geological Survey Miscellaneous Investigations Series Map I-2295*, scale
1081 1:25,000. <https://doi.org/10.3133/i2295>
- 1082 Ross DC (1989) The metamorphic and plutonic rocks of the southernmost Sierra Nevada, California, and
1083 their tectonic framework. *US Geol Surv Prof Pap* 1381. <https://doi.org/10.3133/pp1381>
- 1084 Ross DC (1988) Chemical traits and trends of the granitic rocks of the southern Sierra Nevada, California.
1085 *USGS Open File Report OFR-88-374*. <https://doi.org/10.3133/ofr88374>
- 1086 Ross DC (1987) Mafic plutonic rocks of the southern Sierra Nevada, California. *USGS Open-File Report*
1087 87-275. <https://doi.org/10.3133/ofr87275>
- 1088 Ross DC (1985) Mafic gneissic complex (batholithic root?) in the southernmost Sierra Nevada, California.
1089 *Geology* 13:288–291. [https://doi.org/10.1130/0091-7613\(1985\)13<288:MGCBRI>2.0.CO;2](https://doi.org/10.1130/0091-7613(1985)13<288:MGCBRI>2.0.CO;2)
- 1090 Rudnick RL, Fountain DM (1995) Nature and composition of the continental crust: A lower crustal
1091 perspective. *Rev Geophys* 33:267. <https://doi.org/10.1029/95RG01302>
- 1092 Ruppert S, Fliedner MM, Zandt G (1998) Thin crust and active upper mantle beneath the Southern Sierra
1093 Nevada in the western United States. *Tectonophysics* 286:237–252. [https://doi.org/10.1016/S0040-1951\(97\)00268-0](https://doi.org/10.1016/S0040-1951(97)00268-0)
- 1094
- 1095 Saleeby J, Ducea M, Clemens-Knott D (2003) Production and loss of high-density batholithic root,
1096 southern Sierra Nevada, California. *Tectonics* 22. <https://doi.org/10.1029/2002TC001374>
- 1097 Saleeby J, Farley KA, Kistler RW, Fleck RJ (2007) Thermal evolution and exhumation of deep-level
1098 batholithic exposures, southernmost Sierra Nevada, California. *Spec Pap 419 Convergent Margin Terranes*
1099 *Assoc Reg A Tribute to WG Ernst* 2419:39–66. [https://doi.org/10.1130/2007.2419\(02\)](https://doi.org/10.1130/2007.2419(02))
- 1100 Saleeby JB, Ducea MN, Busby CJ, Nadin ES, Wetmore PH (2008) Chronology of pluton emplacement and
1101 regional deformation in the southern Sierra Nevada batholith, California. *Spec Pap 438 Ophiolites,*
1102 *Arcs, Batholiths A Tribute to Cliff Hopson* 2438:397–427. [https://doi.org/10.1130/2008.2438\(14\)](https://doi.org/10.1130/2008.2438(14))
- 1103 Saleeby JB, Sams DB, Kistler RW (1987) U/Pb zircon, strontium, and oxygen isotopic and
1104 geochronological study of the southernmost Sierra Nevada batholith, California (USA). *J Geophys Res*
1105 92:443–466. <https://doi.org/10.1029/JB092iB10p10443>
- 1106 Sams DB (1986) U/Pb zircon geochronology, petrology, and structural geology of the crystalline rocks of
1107 the southernmost Sierra Nevada and Tehachapi Mountains, Kern County, California. PhD thesis, Calif
1108 Inst Tech, Pasadena
- 1109 Sawyer EW (2000) Grain-scale and outcrop-scale distribution and movement of melt in a crystallising
1110 granite. *Earth and Environmental Science Transactions of the Royal Society of Edinburgh*, 91:73–85.
1111 10.1017/S0263593300007306
- 1112 Schmidt MW (1992) Amphibole composition in tonalite as a function of pressure: an experimental
1113 calibration of the Al-in-hornblende barometer. *Contrib to Mineral Petrol* 110:304–310.
1114 <https://doi.org/10.1007/BF00310745>
- 1115 Schmidt MW, Jagoutz O (2017) The global systematics of primitive arc melts. *Geochemistry, Geophys*

- 1116 Geosystems 18:2817–2854. <https://doi.org/10.1002/2016GC006699>
- 1117 Sisson TW, Grove TL (1993) Experimental investigations of the role of H₂O in calc-alkaline
- 1118 differentiation and subduction zone magmatism. *Contrib to Mineral Petrol* 113:143–166.
- 1119 <https://doi.org/10.1007/BF00283225>
- 1120 Sisson TW, Ratajeski K, Hankins WB, Glazner AF (2005) Voluminous granitic magmas from common
- 1121 basaltic sources. *Contrib to Mineral Petrol* 148:635–661. <https://doi.org/10.1007/s00410-004-0632-9>
- 1122 Sparks RSJ, Marshall LA (1986) Thermal and mechanical constraints on mixing between mafic and silicic
- 1123 magmas. *J Volcanol Geotherm Res* 29:99–124. [https://doi.org/10.1016/0377-0273\(86\)90041-7](https://doi.org/10.1016/0377-0273(86)90041-7)
- 1124 Tamura Y (1994) Genesis of island arc magmas by mantle-derived bimodal magmatism: Evidence from the
- 1125 shirahama group, Japan. *J Petrol* 35(3), 619–645. 10.1093/petrology/35.3.619.
- 1126 Tamura Y, Ishizuka O, Stern RJ, Shukuno H, Kawabata H, Embley RW, Hirahara Y, Chang Q, Kimura J-I,
- 1127 Tatsumi Y, Nunokawa A, Bloomer SH (2011) Two Primary Basalt Magma Types from Northwest
- 1128 Rota-1 Volcano, Mariana Arc and its Mantle Diapir or Mantle Wedge Plume. *J Petrol* 52(6), 1143–
- 1129 1183. 10.1093/petrology/egr022.
- 1130 Tamura Y, Tani K, Chang Q, Shukuno H, Kawabata H, Ishizuka O, Fiske RS (2007) Wet and dry basalt
- 1131 magma evolution at Torishima volcano, Izu-Bonin arc, Japan: The possible role of phengite in the
- 1132 downgoing slab. *J Petrol* 48(10), 1999–2031. 10.1093/petrology/egm048.
- 1133 Tamura Y, Tani K, Ishizuka O, Chang Q, Shukuno H, Fiske RS (2005) Are Arc Basalts Dry, Wet, or Both?
- 1134 Evidence from the Sumisu Caldera Volcano, Izu–Bonin Arc, Japan. *J Petrol* 46(9), 1769–1803.
- 1135 10.1093/petrology/egi033.
- 1136 Tatsumi Y Suzuki T (2009) Tholeiitic vs calc-alkalic differentiation and evolution of arc crust: constraints
- 1137 from melting experiments on a basalt from the Izu–Bonin–Mariana Arc. *J Petrol* 50:1575–1603.
- 1138 <https://doi.org/10.1093/petrology/egp044>
- 1139 Tavazzani L, Peres S, Sinigoi S, Demarchi G, Economos RC, Quick JE (2020) Timescales and
- 1140 Mechanisms of Crystal-mush Rejuvenation and Melt Extraction Recorded in Permian Plutonic and
- 1141 Volcanic Rocks of the Sesia Magmatic System (Southern Alps, Italy). *J. Petrol*
- 1142 doi:10.1093/petrology/egaa049
- 1143 Taylor SR, McLennan SM (1995) The geochemical evolution of the continental crust. *Rev. Geophys*
- 1144 33:241–265. <https://doi.org/10.1029/95RG00262>
- 1145 Tolan PME, Bindeman I, Blundy JD (2012) Cumulate xenoliths from St. Vincent, Lesser Antilles Island
- 1146 Arc: A window into upper crustal differentiation of mantle-derived basalts. *Contrib to Mineral Petrol*
- 1147 163:189–208. <https://doi.org/10.1007/s00410-011-0665-9>
- 1148 Tormey DR, Grove TL, Bryan WB (1987) Experimental petrology of normal MORB near the Kane
- 1149 Fracture Zone: 22°–25° N, mid-Atlantic ridge. *Contrib to Mineral Petrol* 96:121–139.
- 1150 <https://doi.org/10.1007/BF00375227>
- 1151 Tuttle, Bowen (1958) Origin of Granite in the Light of Experimental Studies in the System NaAlSi₃O₈–
- 1152 KAlSi₃O₈–SiO₂–H₂O. *Geological Society of America* 74. <https://doi.org/10.1130/MEM74>

- 1153 Ulmer P, Kaegi R, Müntener O (2018) Experimentally Derived Intermediate to Silica-rich Arc Magmas by
1154 Fractional and Equilibrium Crystallization at 1.0 GPa: an Evaluation of Phase Relationships,
1155 Compositions, Liquid Lines of Descent and Oxygen Fugacity. *J Petrol* 59:11–58.
1156 <https://doi.org/10.1093/petrology/egy017>
- 1157 Ushioda M, Takahashi E, Hamada M, Suzuki T (2014) Water content in arc basaltic magma in the
1158 Northeast Japan and Izu arcs: An estimate from Ca/Na partitioning between plagioclase and melt. *Earth,*
1159 *Planets Sp* 66:1–10. <https://doi.org/10.1186/1880-5981-66-127>
- 1160 Villiger S, Ulmer P, Muntener O (2007) Equilibrium and Fractional Crystallization Experiments at 0.7
1161 GPa; the Effect of Pressure on Phase Relations and Liquid Compositions of Tholeiitic Magmas. *J Petrol*
1162 48:159–184. <https://doi.org/10.1093/petrology/egl058>
- 1163 Villiger S, Ulmer P, Müntener O, Thompson AB (2004) The Liquid Line of Descent of Anhydrous,
1164 Mantle-Derived, Tholeiitic Liquids by Fractional and Equilibrium Crystallization-an Experimental
1165 Study at 1.0 GPa. *J Petrol* 45:2369–2388. <https://doi.org/10.1093/petrology/egh042>
- 1166 Walker BA, Bergantz GW, Otamendi JE, Ducea MN, Cristofolini EA (2015) A MASH Zone Revealed: the
1167 Mafic Complex of the Sierra Valle Fértil. *J Petrol* 56:1863–1896.
1168 <https://doi.org/10.1093/petrology/egv057>
- 1169 Wanke M., Clynne MA., von Quadt A, Vennemann TW, Bachmann O. (2019). Geochemical and
1170 petrological diversity of mafic magmas from Mount St. Helens. *Contrib Mineral Petrol* 174, 10
1171 [.https://doi.org/10.1007/s00410-018-1544-4](https://doi.org/10.1007/s00410-018-1544-4)
- 1172 Weinberg RF, Vernon RH, Schmeling H (2021) Processes in mushes and their role in the differentiation of
1173 granitic rocks. *Earth-Science Rev* 103665. <https://doi.org/10.1016/j.earscirev.2021.103665>
- 1174 Wernicke B, Clayton R, Ducea M, Jones CH, Park S, Ruppert S, Saleeby JB, Snow JK, Squires L,
1175 FLiedner M, Jiracek G, Keller R, Klempere S, Luetgert J, Malin P, Miller K, Mooney W, Oliver H,
1176 Phinney R (1996) Origin of high mountains in the continents: The Southern Sierra Nevada. *Science*
1177 271:190-193. <https://doi.org/10.1126/science.271.5246.190>
- 1178 White AJR, Chappell BW (1983) Granitoid types and their distribution in the Lachlan Fold Belt,
1179 southeastern Australia. *Mem Geol Soc Am* 159. <https://doi.org/10.1130/MEM159-p21>
- 1180 Wood DJ, Saleeby JB (1997) Late Cretaceous-Paleocene Extensional Collapse and Disaggregation of the
1181 Southernmost Sierra Nevada Batholith. *Int Geol Rev* 39:973–1009.
1182 <https://doi.org/10.1080/00206819709465314>
- 1183 Zimmer MM, Plank T, Hauri EH, Yogodzinski GM, Stelling P, Larsen J, Singer B, Jicha B, Mandeville C,
1184 Nye CJ (2010) The Role of Water in Generating the Calc-alkaline Trend: New Volatile Data for
1185 Aleutian Magmas and a New Tholeiitic Index. *J Petrol* 51:2411–2444.
1186 <https://doi.org/10.1093/petrology/egq062>



1188

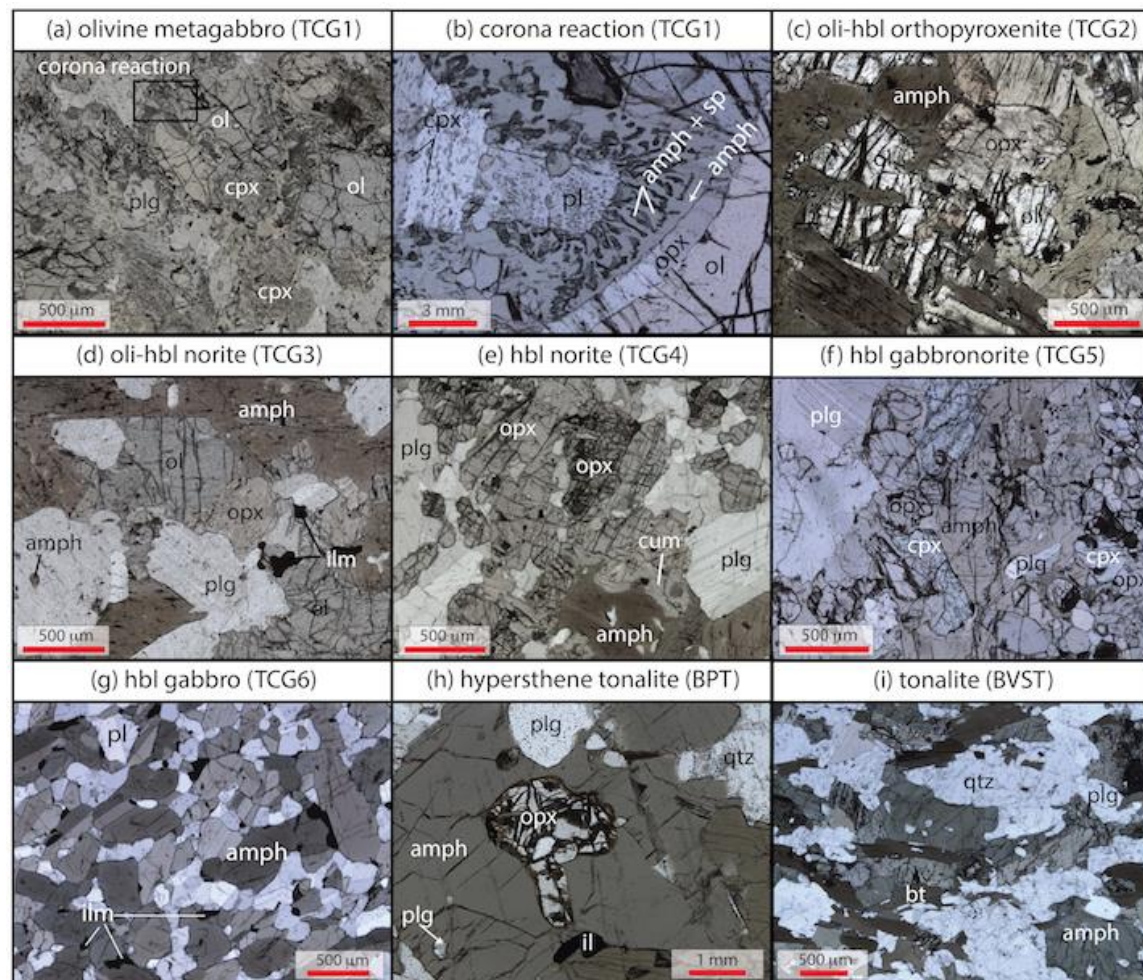


Figure 2

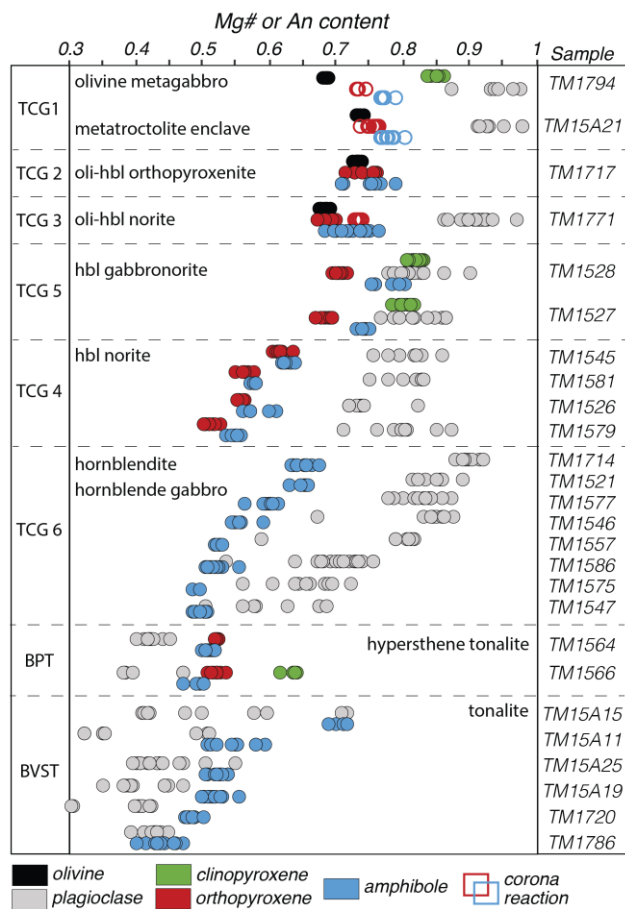


Figure 3

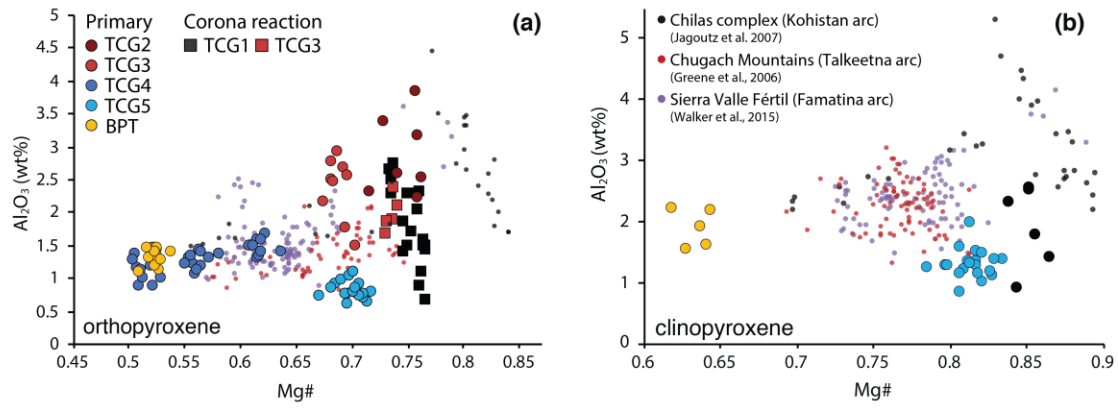


Figure 4

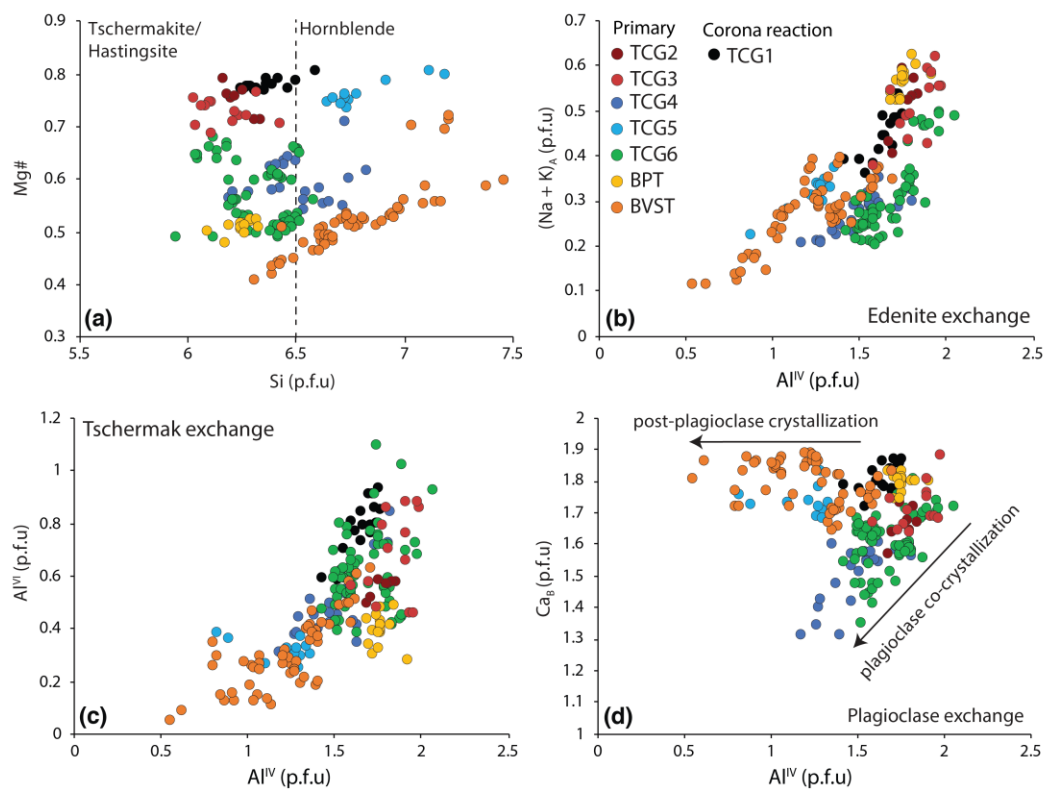


Figure 5

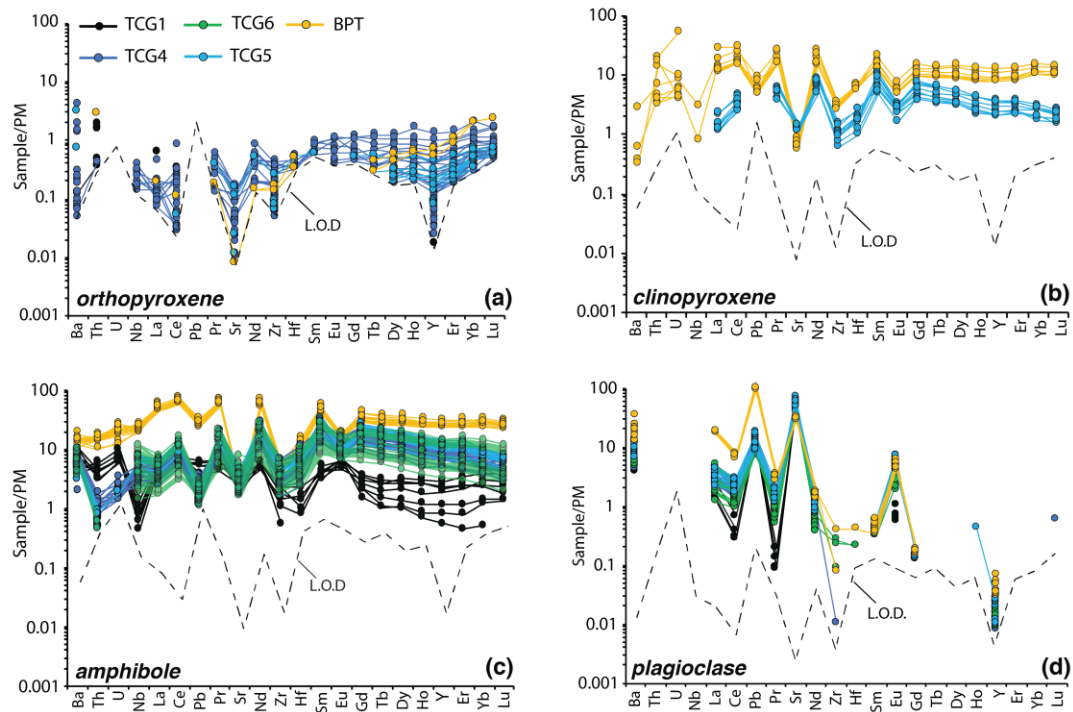


Figure 6

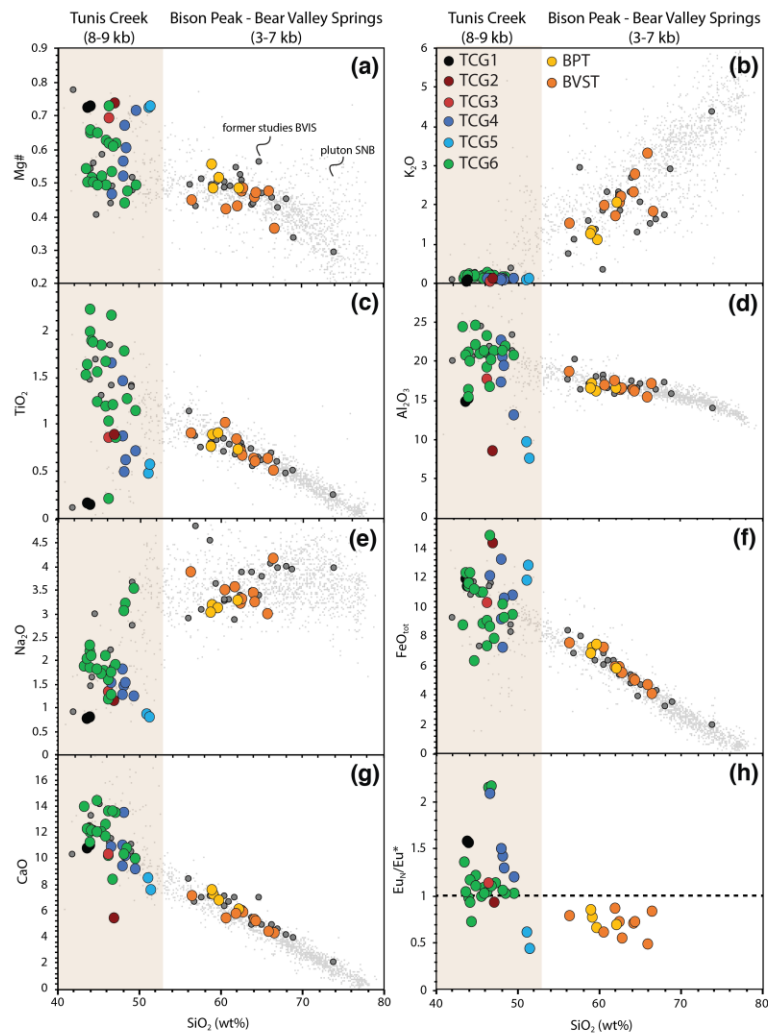


Figure 7: Bulk rock major element

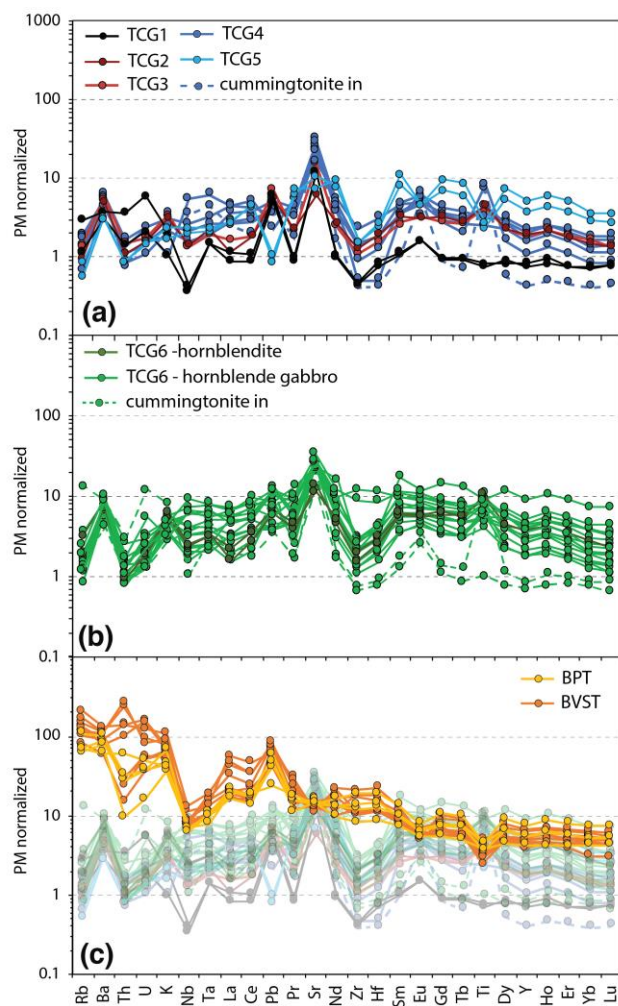


Figure 8: Bulk rock trace element

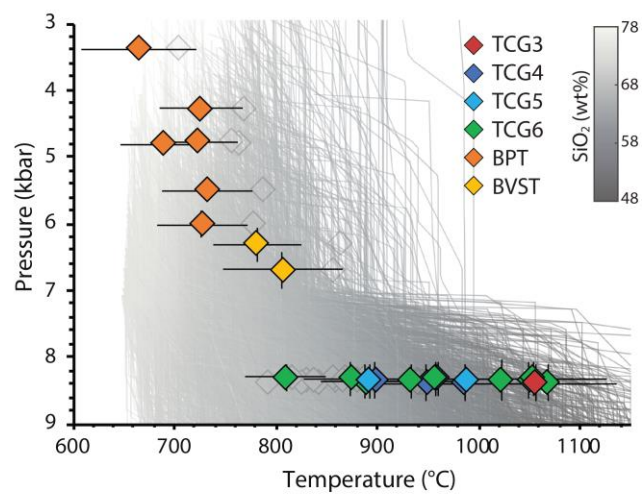


Figure 9

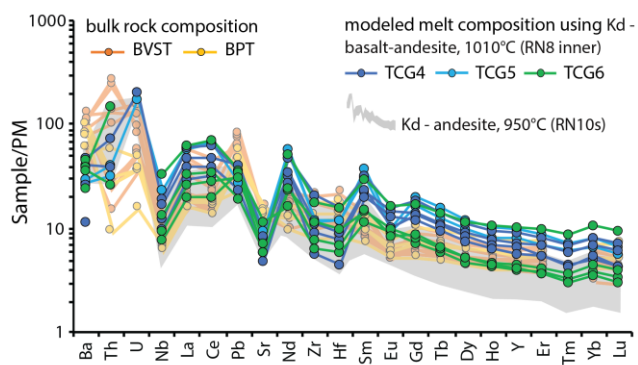


Figure 10: amphibole trace element modelling

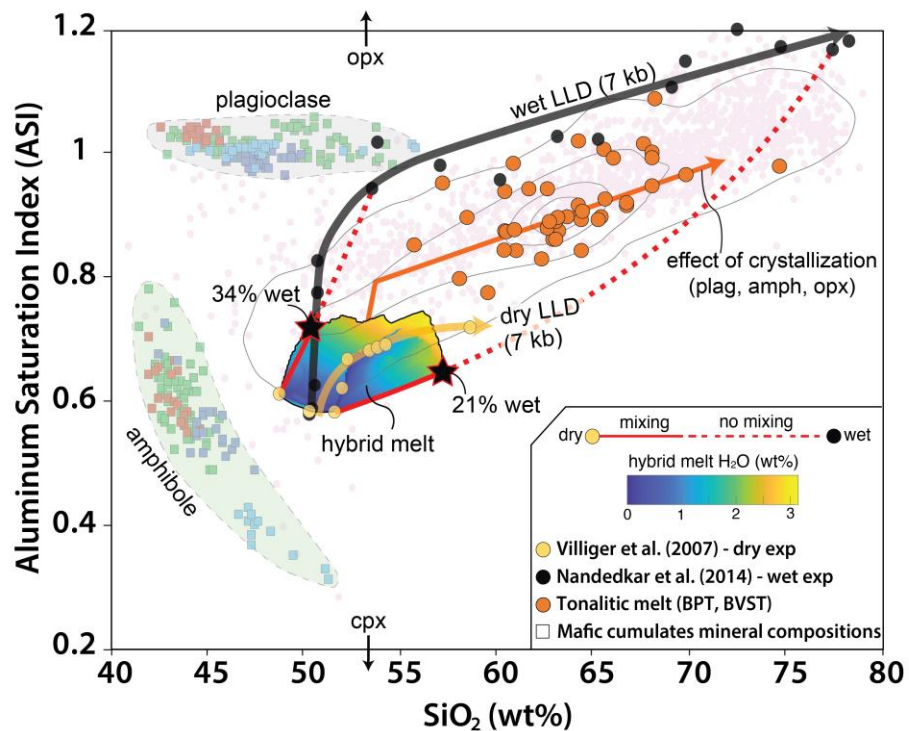


Figure 11

1198

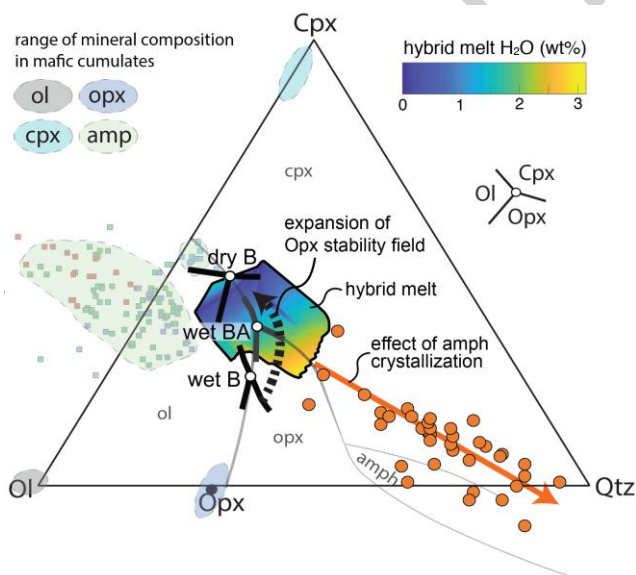


Figure 12

1199

1200

Table 1: Summary of petrographic descriptions

Group	Unit	Rock type / Sequence of mineral crystallization	Petrography
TCG1	Tunis Creek / Bear Valley Springs	Olivine metagabbro/Metatroctolite enclave ol → cpx → plag (corona: opx → amph → spinel)	Olivine metagabbro is composed of sub-euhedral olivine, plagioclase, and altered clinopyroxene (Fig. 2B). Clinopyroxene also occurs as tiny inclusions (15-20 µm) in plagioclase indicative of clinopyroxene crystallization before plagioclase (Fig. 2B). The tonalite-hosted metatroctolite enclave consists of olivine and plagioclase with tiny inclusions of clinopyroxene. For each gabbro, the relative abundance of plagioclase and olivine varies amongst samples due to the presence of multi-layered corona textures of variable thicknesses. The metagabbro is composed of an inner corona of orthopyroxene at the contact with olivine overgrown by an outer corona of green amphibole that progressively co-crystallized with rare clinopyroxene and green spinel symplectites at the contact with plagioclase (Fig. 2B). Pickett and Saleeby (1993) reported similar texture in Tunis Creek gabbro.
TCG2	Tunis Creek	Olivine-hornblende orthopyroxenite ol → opx → amph	Olivine occurs in small amount, while beige to reddish subeuhedral orthopyroxene and brown amphibole co-crystallized in equal proportions (Fig. 2c). Amphibole oikocrysts hosting both orthopyroxene and olivine indicate late amphibole crystallization with respect to orthopyroxene and olivine. Both orthopyroxene and amphibole exhibit exsolution trails of Fe-Ti oxides (Fig. 2c).
TCG3	Tunis Creek	Olivine-hornblende norite ol → opx + amph + plag	Olivine occurs in smaller amount compared to reddish to pale green pleochroic subeuhedral orthopyroxene and large brown to beige amphibole and plagioclase (Fig. 2d). The occurrences of triple junctions between orthopyroxene, amphibole and plagioclase suggest equilibrium textures. We also observe resorbed olivine indicative of early crystallization. Orthopyroxene, plagioclase and amphibole are found as inclusions in each other phases indicative of late crystallization. Ilmenite occurs at mineral interfaces (Fig. 2d), while orthopyroxene and amphibole exhibit exsolution trails of Fe-Ti oxides.
TCG4	Tunis Creek	Hornblende norite plag + opx → amph	Reddish to pale green pleochroic subeuhedral orthopyroxenes and plagioclase are the major phases. Amphibole inclusions suggesting co-crystallization of orthopyroxene and plagioclase (Fig. 2e). Amphibole growth at the expense of orthopyroxene and host plagioclase inclusions indicative of late crystallization. Clinopyroxene is observed as a subsolidus reaction at the interface between orthopyroxene and hornblende (Fig. 2f).
TCG5	Tunis Creek	Hornblende gabbro/norite plag + opx + cpx → amph	Hornblende gabbro/norite is composed of pyroxene-rich layers characterized by a granoblastic texture. Rare resorbed plagioclase suggestive of plagioclase crystallization prior to pyroxenes. Amphibole oikocrysts with interstitial phase with resorbed pyroxenes and plagioclase inclusions (Fig. 2f). Fe-Ti oxides are rare.
TCG6	Tunis Creek	Hornblende/gabbro px → amph → plag	Hornblende consists of large amphibole hosting rare remnants of pyroxene in amphibole and the resorbed interstitial plagioclase. Amphibole crystals display patchy zoning and Fe-Ti oxides exsolution trails. Hornblende gabbro is composed of sub-euhedral to euhedral dark green to beige amphibole and plagioclase in variable proportions with Fe-Ti oxides (Fig. 2g). Remnants of pyroxene are rare in amphibole. Plagioclase inclusions in amphibole and vice versa are commonly observed, suggesting co-crystallization. Amphibole exhibit subsolidus exsolution trails of Fe-Ti oxides and cummingtonite.
BP	Bison Peak	Hypersthene Tonalite plag + px → amph + bt → qtz + Kspar	It is composed of plagioclase, amphibole, biotite, pyroxene, K-feldspar and Fe-Ti oxides, where dark green amphibole crystallized at the expense of remnant crystals of orthopyroxene and rare clinopyroxene. Plagioclase rarely display a sieve-textured core, and clusters of biotite and Fe-Ti oxides surround amphibole. Limited quartz recrystallization suggests minor deformation.
BVS	Bear Valley Springs	Tonalite plag → amph + bt → qtz + Kspar	It is dominated by plagioclase, quartz, and K-feldspar together with interstitial green amphibole and Fe-Ti oxides (Fig. 2i). Few samples contain plagioclase with sieve-textured cores.

Mineral abbreviations: amph – amphibole; bt – biotite; cpx – clinopyroxene; kspar – K feldspar; ol – olivine; opx – orthopyroxene; plag – plagioclase; px – pyroxene; qtz – quartz

1201

1202

1203

1204

Table 2: Summary of calculated intensive parameters for the Bear Valley intrusive suite

Type	Sample	Texture	T (°C) ¹	T _{error}	T (°C) ²	T _{error}	T (°C) ³	T _{liquidus} (°C) ⁴	P (kbar) ⁵	P _{error}	P (kbar) ⁶	P (kbar) ³
		<i>amphibole</i>		<i>amph-only</i>		<i>plag-amph pair</i>	<i>2 px</i>	<i>olivine</i>	<i>Interpolated P surface</i>		<i>Al-in amphib</i>	<i>2 px</i>
TCG1	TM1794	Corona	942.6	30.5	-			1070-1097	8.33	0.28		
TCG1	TM15A21	Corona	906.4	31.1	-			1087-1114				
TCG2	TM1717	Oikocryst	944.6	32.7	-			1086-1113	8.39	0.27		
TCG3	TM1771	Oikocryst	946.3	33.3	1055.4	55.6		1069-1096	8.39	0.27		
TCG4	TM1545	Interstitial	868.5	31.4	959.7	43.2			8.32	0.26		
TCG4	TM1579	Interstitial	792.7	33.9	949.0	42.4			8.39	0.27		
TCG4	TM1581	Interstitial	844.0	43.4	985.5	43.2			8.38	0.27		
TCG4	TM1526	Interstitial	830.1	54.3	898.3	43.5			8.34	0.26		

TCG5	TM1527	Interstitial	868.0	30.7	986.6	44.9	910.7		8.35	0.26		11.0
TCG5	TM1528	Interstitial	838.9	42.6	892.1	44.1	882.7		8.35	0.26		9.4
TCG6	TM1714	sub-euhedral	941.1	30.2	1067.7	45.3			8.39	0.27		
TCG6	TM1586	sub-euhedral	827.4	30.5	888.6	41.8			8.36	0.27		
TCG6	TM1577	sub-euhedral	859.2	37.4	932.4	48.4			8.35	0.26		
TCG6	TM1575	sub-euhedral	856.7	34.5	809.6	40.2			8.3	0.2		
TCG6	TM1547	sub-euhedral	816.1	31.5	873.5	43.2			8.32	0.26		
TCG6	TM1546	sub-euhedral	889.5	30.1	1053.7	49.0			8.32	0.26		
TCG6	TM1557	sub-euhedral	870.0	30.0	957.3	43.2			8.32	0.26		
TCG6	TM1521	sub-euhedral	882.4	35.6	1050.3	49.5			8.34	0.26		
TCG6	TM1719	sub-euhedral	898.2	30.4	1022.1	72.9			8.34	0.3		
BPT	TM1566	rimming px	858.3	31.4	806.5	55.3			6.69	0.27	7.3	
BPT	TM1564	rimming px	864.6	30.3	781.6	40.9			6.31	0.26	7.2	
BVST	TM1786	Interstitial	786.7	30.9	731.4	42.0			5.5	0.17	6.6	
BVST	TM15A25	Interstitial	755.8	30.8	722.7	40.2			4.76	0.14	3.7	
BVST	TM15A15	Interstitial	763.0	32.8	688.1	40.3			4.8	0.15	2.4	
BVST	TM15A11	Interstitial	704.3	34.0	664.8	47.5			3.37	0.17	2.3	
BVST	TM15A19	Interstitial	767.6	32.4	725.4	40.4			4.27	0.13	4.1	
BVST	TM1720	Interstitial	777.2	30.5	727.3	42.1			6.01	0.2	5.6	

abbreviations: amph: amphibole; plag: plagioclase; px: pyroxene

¹calculated after Putirka (2016) with an uncertainty of $\pm 30^{\circ}\text{C}$

²calculated after Holland & Blundy (1994) with an uncertainty of $\pm 40^{\circ}\text{C}$ - equation (B) using Pressure from Klein et al. (2021)

³calculated after Putirka (2008) using equation (36) for temperature (39) for pressure with a standard error of 45°C and 3.7 kbars.

⁴calculation of olivine liquidus in dry melt from Niu et al.(2002) - $T(^{\circ}\text{C}) = 1066 + 12.067 \text{ Mg}_{\text{melt}}^{\#} + 312.3 (\text{Mg}_{\text{melt}}^{\#})^2$ and subsequently corrected for the effect of H_2O assuming 2-3 wt% H_2O after Médard & Grove (2008) - $\Delta T(^{\circ}\text{C}) = 40.4 * (\text{melt } \text{H}_2\text{O}) - 2.97 * (\text{melt } \text{H}_2\text{O})^2 + 0.0761 * (\text{melt } \text{H}_2\text{O})^3$ and the effect of pressure after Herzberg & O'Hara (2002) - $T_{\text{pcorr}} = T + 54P - P^2$

⁵after Klein et al. (2021) from interpolated pressure surface following the methods of Nadin and Saleeby (2008) and Chapman et al. (2012).

⁶calculated after Schmidt (1992) - $P (\pm 0.6 \text{ kbars}) = -3.01 + 4.76 \text{Al}^{\text{tot}}$

1205
1206